

Reviewed Preprint

v1 • July 10, 2026

Not revised

✉ For correspondence:

dic2009@med.cornell.edu

Competing interests: No

competing interests declared

Funding: See page 22

Reviewing editor: Justin Trotter,
Stanford University, United States

© 2026, Lituma et al. This article is distributed under the terms of the [Creative Commons Attribution License](#), which permits unrestricted use and redistribution provided that the original author and source are credited.

Astrocytic Nonsense-mediated mRNA decay regulates calcium signaling to support synapse function and restrain anxiety

Pablo J Lituma¹, Aykut Deveci¹, Estibaliz Barrio-Alonso¹, Kun Tan^{3,4}, Miles F Wilkinson^{3,4}, Pablo E Castillo^{5,6}, Dilek Colak^{1,2}✉

¹Center for Neurogenetics, Feil Family Brain and Mind Research Institute, Weill Cornell Medical College, Cornell University, New York, United States • ²Gale & Ira Drukier Institute of Children's Health, Weill Cornell Medical College, Cornell University, New York, United States • ³Department of Obstetrics, Gynecology, and Reproductive Sciences, School of Medicine, University of California, San Diego, La Jolla, United States • ⁴Institute of Genomic Medicine, University of California, San Diego, La Jolla, United States • ⁵Dominick P. Purpura Department of Neuroscience, Albert Einstein College of Medicine, Bronx, United States • ⁶Department of Psychiatry and Behavioral Sciences, Albert Einstein College of Medicine, Bronx, United States

eLife Assessment

This **important** study provides the first in vivo evidence that nonsense-mediated mRNA decay (NMD) in mature astrocytes regulates astrocyte function, synaptic plasticity, and anxiety-related behavior. Using a broad range of approaches, the authors show that conditional deletion of *Upf2* alters astrocyte morphology and calcium signaling while impairing synaptic transmission and plasticity, providing **solid** support for the central conclusion that astrocytic NMD influences neural circuit function. Some key mechanistic claims remain **incompletely** supported, including whether phenotypes reflect astrocyte remodeling versus loss, the interpretation of synaptic engulfment data, the link between NMD targets and calcium signaling, and the extent to which calcium dysregulation explains the observed synaptic and behavioral effects.

<https://doi.org/10.7554/eLife.111940.1.sa4>

Abstract

How astrocytes achieve their diverse roles in the brain at the molecular level is poorly understood. In this study, we leverage mouse models, electrophysiology, calcium imaging, behavioral assays, and bioinformatic approaches to demonstrate that astrocyte activity and astrocyte-mediated mouse behavior depends on the highly conserved and selective RNA turnover pathway-nonsense-mediated RNA decay (NMD). Conditional deletion of the core NMD gene, *Upf2*, in mature astrocytes leads to enhanced basal Ca^{2+} signaling coupled with synapse dysfunction and elevated anxiety. Restoring basal Ca^{2+} signaling in NMD-deficient astrocytes rescued synaptic transmission and minimized anxiety-associated behavior. Molecular bioinformatic analysis identified specific NMD target transcripts in astrocytes as candidates influencing calcium signaling pathways and neuroglia interactions that support brain function. Our study is the first to demonstrate specific roles for NMD in astrocytes.

Introduction

Astrocytes are highly communicative. A single mouse cortical astrocyte can contact ~100,000 synapses (1). This number has been suggested to reach up to 2,000,000 synapses for a human astrocyte (2). Thus, astroglia cells are in powerful position to monitor and respond to neural circuit dynamics. Astrocytes detect synaptic activity via membrane transporters and receptors that elevate intracellular Ca^{2+} levels as a means to activate downstream signaling pathways that then trigger release of gliotransmitters and other molecules to modulate neuronal excitability and synaptic function (3–6). Astrocytes also have other functions, including synapse engulfment and autophagy, both of which are critical for neural circuit homeostasis, and, if faulty, contribute to neurodegenerative brain states in adulthood (7, 8).

The molecular pathways underlying astrocyte's diverse functions are poorly understood. An attractive molecular mechanism that has the potential to have a role in spatially- and temporally-restricted activities in astrocytes is post-transcriptional regulation. Deficits in post-transcriptional regulation in neurons are known to result in ectopic protein synthesis and lead to developmental and cognitive disabilities (9–15). Meanwhile, the impact of disrupted post-transcriptional regulation influencing mRNA stability in astrocytes and other brain cell-types remains to be elucidated (16, 17). The best characterized RNA turnover pathway is nonsense-mediated RNA decay (NMD) (18–20). This highly conserved and selective RNA degradation mechanism was first discovered because of its ability to degrade aberrant mRNAs harboring mutations that create premature termination codons (PTCs). NMD was subsequently found to increase the decay rate of subsets of normal mRNAs (21). These normal mRNAs harbor “NMD-inducing features”—such as an exon-exon junction downstream of the main open reading frame (ORF) and long 3' untranslated regions (UTRs)—that trigger their decay via NMD (21–23). The discovery that NMD destabilizes many normal mRNAs has led to the hypothesis that NMD regulates normal biological events, a hypothesis that has been supported by a plethora of studies showing that NMD influences numerous fundamental processes, including development, differentiation, cell cycle regulation, cell survival, stress response, and autophagy (21).

NMD is a complex pathway that depends on many protein factors, including the core NMD factors UPF1, UPF2, and UPF3B (24). In humans, mutations in *UPF3B* have been shown to cause intellectual disability (25–27) and individuals with *UPF3B* mutations often suffer from autism, schizophrenia, and attention-deficit/hyperactivity disorder (25–29), highlighting the crucial role of regulated RNA turnover in the nervous system (25). Similarly, mutations or copy number variants (CNVs) of NMD machinery genes *UPF2*, *UPF3a*, *SMG6* or null mutations of *UPF3B* are associated with neurodevelopmental and neuropsychiatric disorders (21, 24, 25, 27–30). Given that NMD is ubiquitous and NMD target mRNAs are tissue-, cell type-, and NMD factor-specific (31) how NMD dysfunction precisely contributes to brain disorders in humans is unknown. Nonetheless, NMD perturbation via *Upf2* manipulation in neurons using transgenic mice revealed impairments to cell-cycle regulation, cytoarchitecture, axon guidance, synapse activity, and memory function (22, 23, 32–36). Hence, *Upf2* ablation has proven as a versatile tool to further our understanding of NMD function in mammalian cells (37–41). By leveraging *Upf2* transgenic mouse tools, a comprehensive model of how mRNA degradation impacts synaptic and cognitive function can be constructed by dissecting out the role of NMD in all cell types that modulate these brain processes.

To date, no study has reported on roles for NMD in glial cells. To address this important knowledge gap, we conditionally knocked out the NMD gene, *Upf2*, in astrocytes *in vivo*. Implementing cellular and molecular tools, we reveal that astrocytic UPF2-dependent NMD disruption leads to impaired astrocyte cell size and increased Ca^{2+} activity in hippocampus, visual cortex, and prefrontal cortex. These phenotypes are accompanied with impaired synaptic function and anxiety behavior in adult mice. To define a molecular mechanism, using RNA sequencing and an established algorithm that identifies NMD-inducing features in transcripts, we determined the physiological targets of UPF2-dependent NMD in astrocytes. This allowed us to predict the biological pathways regulated by NMD in these cells. NMD targets within astrocytes pointed to morphological remodeling, phagosome formation, and Ca^{2+} signaling. Modulation of Ca^{2+} activity in NMD-

deficient astrocytes *in vivo* restores synaptic function and animal behavior. By characterizing the role of UPF2 dependent-NMD in astrocytes, our study highlights that RNA degradation is a major mechanism that regulates critical astrocytic biological processes required for neuro-glia interactions that ultimately support proper brain function.

Results

Conditional deletion of *Upf2* in astrocytes *in vivo* reduces their size

To determine the physiological requirement for NMD in astrocytes, we leveraged mouse transgenic Cre-lox strategies to ablate the *Upf2* gene in adult mice. *Upf2*^{wt/wt} and *Upf2*^{fl/fl} animals were crossed with the *Aldh1L1-CreER*^{T2} transgenic mouse line to provide temporal control of *Upf2* deletion in astrocytes using tamoxifen. The *Aldh1L1-CreER*^{T2} transgenic mouse line induces CRE expression in astrocytes with high specificity (42) and is widely implemented to study astrocyte functions. To visualize astrocytes and CRE recombination we co-injected the adeno-associated viruses AAV5-GfaABC1D-Lck-GFP and AAV8-GFAP-mCherry-Cre, respectively, into the hippocampus, visual cortex, and prefrontal cortex of CTRL (*Upf2*^{wt/wt}; *Aldh1L1-CreER*^{T2}) and cKO (*Upf2*^{fl/fl}; *Aldh1L1-CreER*^{T2}) mice followed by tamoxifen administration (Figure 1A). Immunohistochemistry confirmed the expression of mCherry-Cre and Lck-GFP across the targeted brain areas (Figure S1). Of note, this experimental design also ensures that phenotypes are not caused by an acute effect of tamoxifen, or a non-specific effect of CRE at cryptic LoxP sites. By anchoring the fluorophore to the membrane, Lck-GFP enables the visualization of fine, ramified branches typically lost in cytosolic imaging, achieving the precision required for morphology analysis. Using spinning disk confocal microscopy, images of Lck-GFP⁺ astrocytes in hippocampus, visual cortex, and prefrontal cortex were acquired (Figure 1A). Imaris 3D reconstructions enabled cell volume and surface area measurements of CTRL and cKO astrocytes across brain regions (Figure 1B). Quantifications revealed that, in all brain regions analyzed, NMD deficiency led to significant reductions in astrocyte cell volume and surface area as compared to CTRL (Figure 1C-D). Our results suggest that NMD regulates astrocyte morphology and raised the possibility that altered astrocyte cell size may impact neuro-glia interactions in *Upf2* cKO brains.

Conditional deletion of *Upf2* in astrocytes *in vivo* disrupts excitatory synapse numbers, spine density, and synapse engulfment

Astrocytes contribute to formation, pruning, and maintenance of synapses in the mammalian central nervous system (7, 43–45). Their unique morphology and interactions with synapses play a crucial role in regulating synapse plasticity and maintenance. Thus, we next sought to determine the impact of astrocytic NMD deficiency on synapse numbers in *Upf2* cKO brains. To facilitate labeling of recombined astrocytes, we employed the Ai6 transgenic mouse line, which drives expression of the ZsGreen1 fluorescent reporter upon CRE recombination. Tamoxifen dosing of *Upf2*^{wt/wt}; *Aldh1L1-CreER*^{T2}; Ai6 (CTRL) or *Upf2*^{fl/fl}; *Aldh1L1CreER*^{T2}; Ai6 (cKO) triple transgenic mice enabled 488 nm fluorescence of recombined astrocytes (Figure 2A).

Immunohistochemistry revealed that ~90% of the astrocyte marker GFAP colocalized with ZsGreen1 in hippocampus and cortex (Figure S2) indicating high recombination rate with successful depletion of UPF2 in these cells (Figure S3). Moreover, ZsGreen1⁺ *Upf2* cKO astrocytes also displayed reduced cell size (Figure S4) supporting our morphological observations using the Lck-GFP reporter. To evaluate synapses, the postsynaptic marker, PSD-95 and lysosomal protein marker, LAMP2 enabled the detection of excitatory synapses and synaptic material in phagocytic compartments of recombined astrocytes (Figure 2A-B). Spinning disk confocal microscopy followed by Imaris 3D reconstructions facilitated the quantification of PSD-95⁺ excitatory synapses as well as engulfment of synaptic material (Figure 2B). Our analysis revealed that *Upf2* cKO brain sections displayed significant reductions in PSD-95 levels associated with low PSD-95/LAMP2⁺ engulfed material across several brain regions when compared to CTRL (Figure 2C-D). The bulk of excitatory synaptic transmission in the brain occurs at dendritic

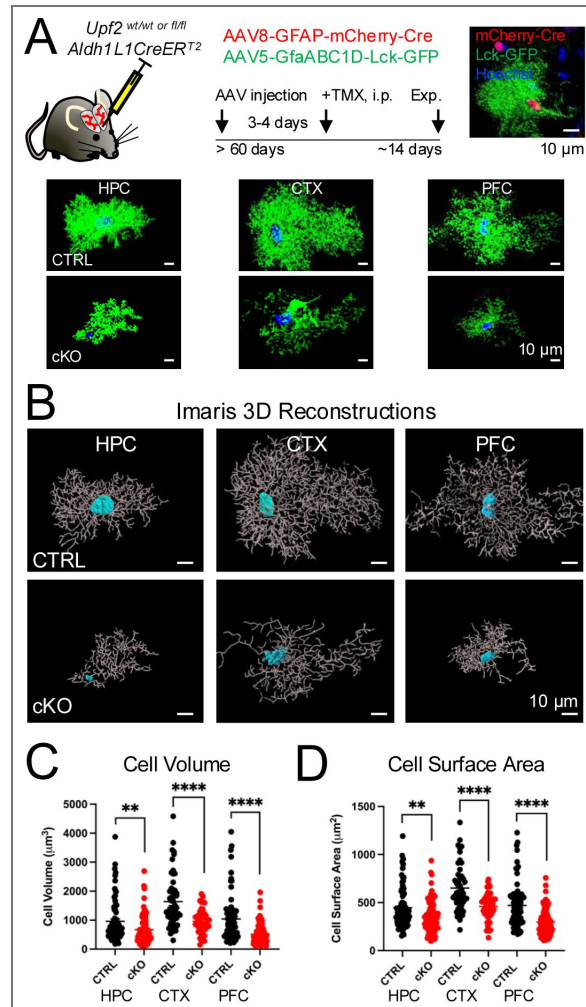


Figure 1. *Upf2* cKO astrocytes show cell size adaptations across brain areas.

(A) Schematic of adeno-associated viral delivery of AAV8-GFAP-mCherry-Cre and AAV5-GfaABC1D.PI.Lck-GFP.SV40 reporters to hippocampus (HPC), visual cortex (CTX), and prefrontal cortex (PFC). Image of mCherry and Lck-GFP expression in region of interest-ROI. Representative astrocyte morphology images from CTRL (top) and *Upf2* cKO (bottom) across targeted brain areas. (B) Imaris 3D reconstructions of CTRL (top) and cKO (bottom) astrocytes from HPC, CTX, and PFC. (C) *Upf2* mutant astrocytes display reduced cell volume as compared to CTRL in HPC, CTX, and PFC (HPC, CTRL: 961 ± 83, 76 cells; cKO: 669 ± 50, 90 cells, $p < 0.001$, Mann-Whitney test. CTX, CTRL: 1639 ± 123, 54 cells; cKO: 959 ± 60, 48 cells, $p < 0.0001$, Mann-Whitney test. PFC, CTRL: 1039 ± 91, 77 cells; cKO: 515 ± 35, 96 cells, $p < 0.0001$, Mann-Whitney test. 3 animals per genotype). (D) *Upf2* mutant astrocytes exhibit decreased cell surface area across brain areas as compared to CTRL (HPC, CTRL: 448 ± 25, 76 cells; cKO: 352 ± 17, 90 cells, $p = 0.002$, Mann-Whitney test. CTX, CTRL: 652 ± 32, 54 cells; cKO: 460 ± 20, 48 cells, $p < 0.0001$, Mann-Whitney test. PFC, CTRL: 471 ± 26, 77 cells; cKO: 297 ± 13, 96 cells, $p < 0.0001$, Mann-Whitney test. 3 animals per genotype). Data is presented as mean ± S.E.M. ** denotes $p < 0.001$ **** denotes $p < 0.0001$. This figure highlights decreased cell volume and surface area in NMD-deficient astrocytes in hippocampus, cortex, and prefrontal cortex.

spines. To determine if reduced synapse numbers are accompanied with alterations in spine densities in *Upf2* cKO brains, we labeled excitatory neurons and their spines by injecting adeno-associated virus AAV5-CamKII α -EGFP to the hippocampus of CTRL (*Upf2*^{wt/wt}, *Aldh1L1-CreER*^{T2}) and cKO (*Upf2*^{fl/fl}, *Aldh1L1-CreER*^{T2}) mice followed by tamoxifen administration (Figure 2E [↗](#)). Quantifications of spine densities revealed a significant decrease in *Upf2* cKO mice as compared to CTRL (Fig. 2E [↗](#)). Taken together, these findings support the hypothesis that UPF2-dependent NMD in astrocytes is essential for proper synapse regulation mediated by these cells.

Conditional deletion of *Upf2* in astrocytes *in vivo* impairs excitatory synaptic function

Synaptic transmission can be either enhanced, through long-term potentiation (LTP), or depressed, through long-term depression (LTD) (46). Given that dendritic spine densities are tightly linked to these long-term plasticity events (47), and we observed reductions both in spine and PSD-95 densities, we hypothesized that basal synaptic transmission and/or synaptic plasticity is altered in *Upf2* cKO conditions. We tested this hypothesis by performing electrophysiology recordings from CTRL and cKO mice. Because LTP and LTD events are well established and widely studied in hippocampus (46, 48, 49), we prepared acute hippocampal slices for CA1 field recordings (Figure 3A [↗](#)). We first assessed basal neurotransmission in the form of input-output curves to probe synaptic strength. Field excitatory postsynaptic potentials (fEPSPs) were elicited by increasing the stimulation intensity while measuring the afferent fiber volley amplitude. In doing so, input-output curves were generated to compare synaptic strength in CTRL and cKO mice. Our results demonstrated that fEPSP slope values were significantly lower in NMD-deficient animals as compared to CTRL (Figure 3B [↗](#)). We also examined presynaptic function by determining the paired-pulse ratio of fEPSP₂/fEPSP₁ synaptic responses. Our analysis revealed no significant differences across genotypes (Figure 3C [↗](#)).

Because LTP magnitude is linked to basal synaptic strength, we next assessed LTP in *Upf2* cKO hippocampus. To do this, we blocked inhibitory transmission using 100 μ M picrotoxin + 3 μ M CGP-555448. A 15 min baseline period of fEPSP slope values was acquired followed by LTP induction using a theta-burst stimulation (TBS) protocol. The last 10 min of fEPSP slope values were normalized to baseline to determine LTP magnitude. Our results indicated that NMD deficiency in astrocytes abolished LTP in comparison to CTRL astrocytes (Figure 3D [↗](#)). We also evaluated LTD by eliciting a low-frequency stimulation (LFS) protocol and found no significant differences in LTD magnitude in cKO slices compared to CTRL slices (Figure 3E [↗](#)).

G-protein coupled receptor (GPCR) LTD and LFS elicited LTD are distinct mechanisms for triggering long-term synaptic plasticity (50, 51). Moreover, previous studies have shown the complex impact of astrocyte signaling on GPCR-mediated LTD phenomena (51). Hence, we induced a GPCR-mediated chemical form of LTD using the Group 1 metabotropic glutamate receptor (mGluR) agonist DHPG (50 μ M, 5 min). Under these experimental conditions, we observed reduced mGluR-LTD magnitude in *Upf2* cKO mice in comparison to CTRL (Figure 3F [↗](#)). Cumulatively, these results indicate that disrupted astrocytic RNA degradation leads to altered synaptic strength and attenuation of specific forms of synaptic plasticity.

Conditional deletion of *Upf2* in astrocytes elicits anxiety behavior in adult mice

The prefrontal cortex, visual cortex, and hippocampus are well-characterized brain regions supporting cognitive functions that influence animal behavior (52–55). The impaired synaptic strength and plasticity in *Upf2*-cKO mice (Figure 3 [↗](#)) led us to hypothesize that disrupted neural circuit activity limited cognitive processing to alter animal behavior. To test this hypothesis, we used an array of behavioral testing paradigms. Prior to initiating behavioral experiments, no difference in animal body weight was detected across test groups (Figure S4A [↗](#)). First, we

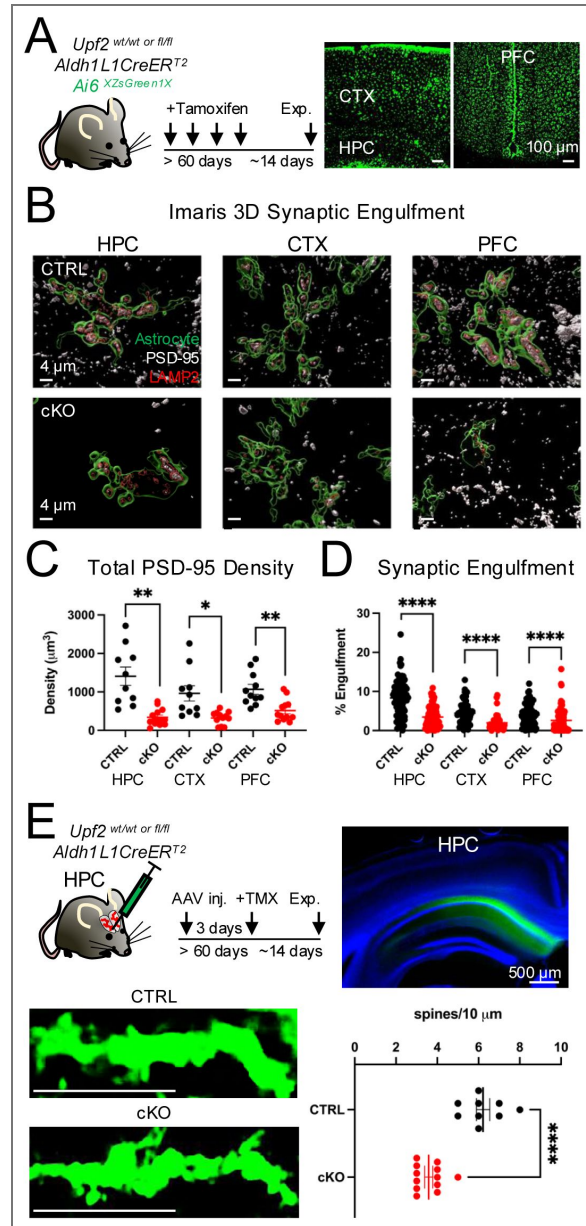


Figure 2. *Upf2* cKO mice display reductions in both PSD-95 and spine density.

(A) Schematic of tamoxifen dosing and images of ZsGreen1 astrocytes in CTX, HPC, and PFC. (B) Imaris 3D rendering of colocalization signals depicting synaptic engulfment represented by PSD-95⁺/LAMP2⁺ puncta in astrocytic field of views (FOVs) across brain regions. (C) UPF2 deficient animals demonstrated reduced PSD-95 signal across brain areas as compared to CTRL (HPC, CTRL: 1409 ± 239, 10 FOVs; cKO: 342 ± 60, 13 FOVs, $p = 0.0014$, Unpaired *t*-test. CTX, CTRL: 963 ± 200, 10 FOVs; cKO: 323 ± 48, 12 FOVs, $p = 0.0011$, Unpaired *t*-test. PFC, CTRL: 1069 ± 129, 11 FOVs; cKO: 516 ± 83, 12 FOVs, $p = 0.002$, Unpaired *t*-test. 3 animals per genotype). (D) *Upf2* mutant astrocytes display minimal synaptic engulfment across brain areas as compared to CTRL (HPC, CTRL: 8.3 ± 0.5, 76 cells, cKO: 3.5 ± 0.3, 90 cells, $p < 0.0001$, Mann-Whitney test. CTX, CTRL: 4.5 ± 0.4, 54 cells, cKO: 1.9 ± 0.3, 48 cells, $p < 0.0001$, Mann-Whitney test. PFC, CTRL: 4.0 ± 0.3, 76 cells, cKO: 2.6 ± 0.3, 97 cells, $p < 0.0001$, Mann-Whitney test. 3 animals per genotype). (E) Schematic of stereotaxic delivery of AAV5-CamKIIα-EGFP virus to label hippocampal CA1 pyramidal neurons (right image) followed by tamoxifen dosing of CTRL and cKO animals. Representative images of dendritic spines in CTRL (top) and cKO (bottom). Scale bar, 10 μm. Astrocytic *Upf2* deficiency is associated with reduced spine density of CA1 pyramidal neurons in comparison to CTRL (CTRL: 6.2 ± 0.3, cKO: 3.6 ± 0.2, $n = 3$ mice per genotype, $p < 0.0001$, Mann-Whitney test). Data is presented as mean ± S.E.M. * denotes $p < 0.05$, ** denotes $p < 0.01$, **** denotes $p < 0.0001$. This figure demonstrates reduced PSD-95 levels associated with decreased spine density of CA1 pyramidal neurons in *Upf2* cKO brains.

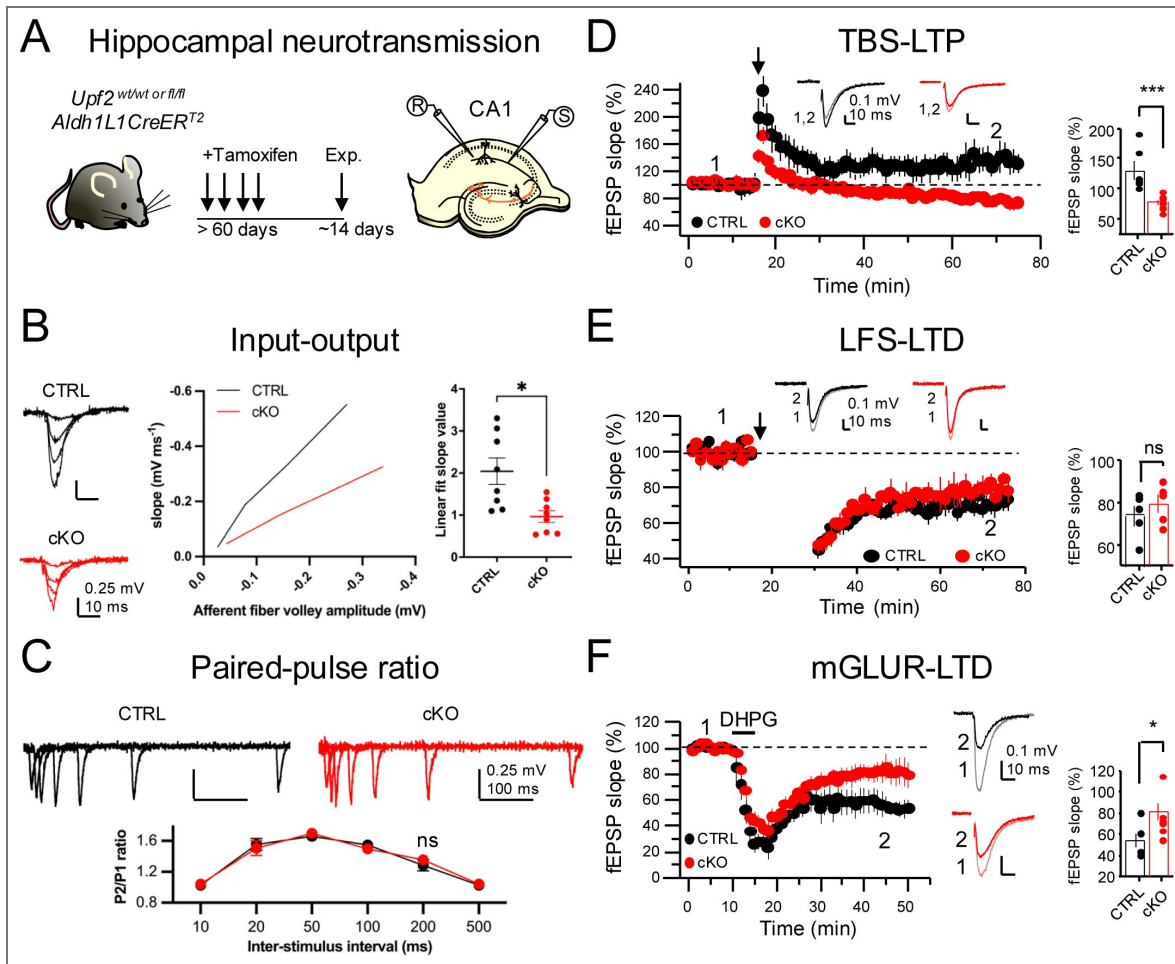


Figure 3. Astrocytic *Upf2* absence impairs basal neurotransmission and synaptic plasticity.

(A) Schematic of tamoxifen dosing and electrophysiology in hippocampal area CA1 of acute brain slices. (B) Input-output curve assessment demonstrated reduced synaptic strength in *Upf2* cKO mice as compared to CTRL (CTRL: Linear fit 2.04 ± 0.3 , $r = 0.99$; cKO: Linear fit 0.96 ± 0.02 , $r = 0.99$, $n = 8$ slices, 4 animals per genotype, linear fit slope values: $p = 0.011$, Unpaired t -test). (C) Presynaptic function assessed by the paired-pulse ratio showed no differences across genotypes (CTRL, 200 ms: 1.3 ± 0.07 ; cKO, 200 ms: 1.35 ± 0.04 , $n = 8$ slices, 4 animals per genotype, $p = 0.4$, Unpaired t -test). (D) LTP induced by theta-burst stimulation led to absent potentiation in the cKO condition (CTRL: $138 \pm 15\%$, $n = 6$ mice, 12 slices; cKO: $78.8 \pm 9\%$, $n = 5$ mice, 9 slices; $p = 0.003$, Unpaired t -test). (E) LTD induced by low-frequency stimulation was similar in both genotypes (CTRL: $72.9 \pm 5\%$; cKO: $78.5 \pm 4\%$, $n = 5$ slices, 3 animals per genotype, $p = 0.41$, Mann-Whitney test). (F) Chemical-LTD induced by DHPG ($50 \mu\text{M}$, 5 min) revealed dampened synaptic depression in *Upf2* cKO brain slices (CTRL: $55.9 \pm 6\%$, $n = 4$ mice, 6 slices; cKO: $84.7 \pm 9\%$, $n = 5$ mice, 7 slices, $p = 0.02$, Unpaired t -test). Data are presented as mean \pm S.E.M. * denotes $p < 0.05$, *** denotes $p < 0.005$, ns = not significant. This figure illustrates that *Upf2* deficiency in astrocytes alters synaptic function.

implemented an Open Field Test to assess general locomotion as previously described (23, 56, 57) across genotypes (Figure 4A). Both groups performed similarly in this test, indicating that general motor activity is not impaired in *Upf2*-cKO mice.

Astrocytes have been reported to modulate anxiety by regulating synaptic activity (58). To test whether *Upf2*-cKO mice have a defect in anxiety behavior, we used the Elevated Plus Maze (EPM) test (59). The EPM test we used contains two open arms and two closed arms, and tests mice's natural curiosity along with their tendency to stay in enclosed spaces and avoid open spaces and heights. Anxious animals will shift the balance away from curiosity and towards safety; thus they will spend more time in the closed arms (59). *Upf2* cKO mice exhibited a strong reduction in time spent in open arms compared to CTRL mice, suggesting they exhibit anxiety-like behavior (Figure 4B).

Astrocytes have also been linked to regulation of repetitive behaviors (60, 61). Thus, we also conducted the marble-burying test. *Upf2* cKO mice buried significantly less marbles compared to CTRL mice (Figure 4C). To further probe repetitive behavior, we implemented the water spray test to induce self-grooming. Similarly, we observed a reduction in self-grooming in cKO mice (Figure S4B). While exhibiting the opposite of repetitive behavior, these results suggest a rather complex behavior with possible modulation of motor activity in specific environmental contexts (62).

Evidence suggests that by fine-tuning LTP, astrocytes promote the formation of new memories (63, 64). Given that LTP is impaired in cKO brains (Figure 3), we tested different aspects of memory. First, we probed short-term memory by implementing the Y-maze that allows an animal to explore two accessible maze arms while a designated third arm (novel arm) is blocked (Figure S4C). No significant differences in novel arm preference index were observed in *Upf2*-cKO mice in comparison to CTRL mice (Figure S4C) suggesting intact short-term memory.

To examine associative memory we performed the 3-day contextual fear conditioning paradigm whereby an animal receives a foot shock (unconditioned stimulus, UC) paired with an auditory tone (conditioned stimulus, CS) in a designated context as previously described (23, 56, 57). On Day 1, UC-CS pairings trigger animals to freeze, the time spent freezing is quantified and interpreted as an animal's ability to execute associative learning. Day 2 measures contextual fear memory, evaluating the animal's freezing behavior in the same context, and Day 3 assesses cued fear memory, testing the animal's response to the tone (CS) that was previously paired with the foot shock (UC). On Day 1, *Upf2*-cKO and CTRL mice displayed similar associative learning aptitude (Figure 4D). To accurately interpret freezing behavior across test days, assessing baseline freezing during the initial epoch across trials is crucial. Intriguingly, *Upf2*-cKO mice exhibited significantly higher baseline freezing responses compared to CTRL mice on Day 2-3 (Figure 4D), a phenotype typically interpreted as elevated baseline fear. Although we detected a significant increase in freezing behavior in *Upf2*-cKO mice during contextual memory assessment (Day 2), pre-existing baseline freezing accompanied with the anxiety phenotype (Figure 4B) impeded an accurate interpretation of associative memory in these mice. Higher baseline freezing has been linked to a rodent model of anxiety (65) consistent with the EPM observation for *Upf2*-cKO mice (Figure 4B). Together, these experiments revealed that astrocytic disruption of UPF2-dependent NMD leads to specific behavioral alterations in adult mice.

Conditional deletion of *Upf2* in astrocytes *in vivo* upregulates mRNAs encoding signaling proteins

While our knowledge of NMD targets in neuronal populations of the central nervous system is growing, the identity and modulation of astrocytic transcripts by NMD is currently unclear (31). To gain mechanistic insight into NMD-mediated astrocyte regulation, we assessed mRNA quantities in NMD-deficient astrocytes. To do this, we isolated recombined hippocampal and cortical astrocytes using Fluorescence Activated Cell Sorting (FACS) from CTRL and cKO animals using ZsGreen1 expression (Figure 5A). Unbiased quantification of recombined cells during sorting determined no differences in sorted cell numbers between the groups (Figure S6A). Additional

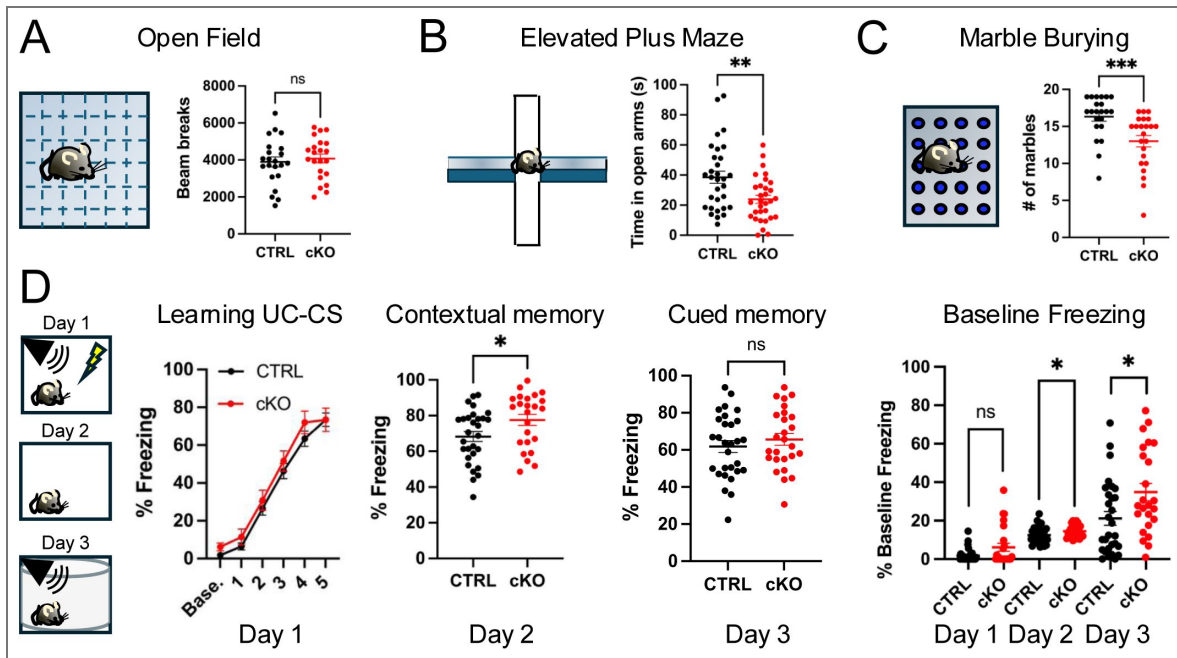


Figure 4. *Upf2* cKO mice display anxiety-like behavior.

(A) Open field beam breaks display no differences in locomotion amongst CTRL and cKO animals (CTRL: 3892 ± 271 ; cKO: 4076 ± 239 , $n = 22$ mice per group, $p = 0.61$, Unpaired t -test). (B) *Upf2* cKO mice show reduced time in open arms of elevated plus maze indicating anxiety-like behavior (CTRL: 38.5 ± 3.9 ; cKO: 23.09 ± 2.6 , $n = 31$ mice per group, $p = 0.0036$, Unpaired t -test). (C) Astrocytic *Upf2* loss is associated with reduced marble burying (CTRL: 16.3 ± 0.6 , $n = 22$ mice; cKO: 13.0 ± 0.8 , $n = 23$ mice, $p = 0.0003$, Mann-Whitney test). (D) Contextual fear conditioning paradigm revealed differences in contextual memory on Day 2 between CTRL and cKO animals (CTRL: 68.3 ± 3 , $n = 29$ mice; cKO: 77.6 ± 3 , $n = 24$ mice, $p = 0.02$, Mann-Whitney test). No differences were detected on Day 1 and Day 3 (Day 1: Baseline vs. UC-CS pairings, CTRL vs. cKO, $p > 0.59$, Sidak's multiple comparisons test; Day 3: CTRL vs. cKO, $p = 0.69$, Unpaired t -test). Assessment of baseline freezing revealed *Upf2* cKO mice show significant elevation on Day 2 and Day 3 as compared to CTRL (Day 1: CTRL: 1.8 ± 0.6 ; cKO: 6.1 ± 2.1 , $p = 0.43$, Mann-Whitney test. Day 2: CTRL: 12.4 ± 0.8 ; cKO: 14.6 ± 0.7 , $p = 0.048$, Unpaired t -test. Day 3: CTRL: 21.2 ± 3.6 ; cKO: 34.9 ± 4.5 , $p = 0.03$, Mann-Whitney test. CTRL: $n = 29$ mice, cKO: $n = 24$ mice). Data are presented as mean \pm S.E.M. * denotes $p < 0.05$, ** denotes $p < 0.01$, *** denotes $p < 0.005$, ns = not significant. This figure illustrates that astrocytic UPF2 depletion is associated with avoidance behavior and increased baseline freezing.

quantification of GFAP⁺ astrocytes in lower layers of cortex and hippocampus revealed no significant difference in cell number across genotypes (Figure S6B). Together, these observations strongly suggested that *Upf2* deletion did not alter cell proliferation or survival.

To identify mRNAs regulated by UPF2, enriched astrocyte populations from cKO and CTRL groups were subjected to RNA sequencing (RNA-seq) analysis (Figure 5B). This analysis identified 277 differentially expressed genes (DEGs; $q < 0.05$, fold change > 2) (Figure 5C; see supplementary data for the full list of DEGs). Because NMD facilitates mRNA degradation, its deficiency is predicted to lead to the accumulation of NMD-target mRNAs. Consistent with this notion, ~93% of the DEGs (257 of 277) exhibited upregulation while only ~7% (20 of 277) were downregulated in cKO astrocytes. The 257 upregulated mRNAs in cKO astrocytes are candidates to be direct NMD targets in these cells. To assess this, we screened them for 3 features mostly known to elicit NMD: an exon-exon junction downstream of the main ORF (a “dEJ”), an ORF upstream of the main ORF (an “uORF”), and a 3'UTR longer than 1,500 nucleotides (nt) (16, 66) (see Introduction). We found that 104 of the upregulated transcripts (40% of the total) contained at least one of these canonical NMD-inducing features (Figure 5D). Thus, these 104 mRNAs are likely NMD target mRNAs in adult cortical and hippocampal astrocytes. Many of the remaining 153 upregulated mRNAs may also be NMD targets; for example, it is known that 3'UTRs shorter than the cut-off length we selected (1,500 nt) can elicit NMD (67–72). It is also possible that some of these upregulated RNAs are indirectly regulated by NMD.

To predict biological functions regulated by NMD in adult astrocytes, we performed Gene Ontology (GO) analysis, which revealed that genes upregulated upon the loss of UPF2 are associated with “glial cell development and differentiation,” “nervous system development,” and “neurogenesis” (Figure 5E). We also performed pathway analysis using Ingenuity Pathway Analysis (IPA), which showed statistically significant enrichment for “leukocyte extravasation signaling,” “phagosome formation,” and “S100 Family and G-protein coupled receptor signaling” (Figure 5F), all of which are linked to Ca²⁺ activity. This raised the possibility that NMD regulates astrocyte Ca²⁺ signaling, which we tested below.

Spontaneous Ca²⁺ activity is elevated in *Upf2*-deleted astrocytes

Astrocytes are known to influence synaptic transmission and plasticity in neurons (3–5, 63) via a Ca²⁺-dependent mechanism, but how precisely this is mediated is not well understood (73–75). Given that we found Ca²⁺-dependent processes are linked with genes regulated by NMD in astrocytes (Figure 5F), we elected to determine whether NMD has an impact on Ca²⁺ signaling in astrocytes. Among the biological pathways predicted to be altered, the S100 and G-protein signaling cascades in *Upf2*-depleted astrocytes (Figure 5F) suggested disrupted Ca²⁺ activity in these cells. To test this, we measured spontaneous Ca²⁺ dynamics upon deletion of *Upf2* in astrocytes *in vivo*. For this, we induced gene deletion in hippocampus, visual cortex, and prefrontal cortex of floxed mice via injection of AAV8-GFAP-mCherry-Cre virus. Simultaneously, we delivered AAV5-GfaABC1D-cyto-GCaMP6f virus to the same brain regions to enable cell visualization (red) and measurement of Ca²⁺ transients (green) using two-photon laser scanning microscopy in acute coronal brain slices (Figure 6A). In the AAV5-GfaABC1D-cyto-GCaMP6f vector, the Ca²⁺ indicator *GCaMP6f* gene is driven by an astrocyte-specific promoter, ensuring its selective expression in these cells, as shown in a previous study (76). To further ensure selective live-imaging of only CRE⁺ astrocytes, the laser wavelength was tuned to 780 nm across brain areas to identify mCherry⁺ regions of interest (Figure S7). Time-lapse imaging enabled the acquisition of spontaneous Ca²⁺ transients reported by cyto-GCaMP6f⁺ astrocytes that facilitated the generation of heat-maps and temporal dynamic traces for Ca²⁺ fluctuations in hippocampus, visual cortex, and prefrontal cortex (Figure 6B–D). Measurements of peak Ca²⁺ amplitude in hippocampus, visual cortex, and prefrontal cortex revealed elevated spontaneous Ca²⁺ activity in *Upf2*-cKO slices as compared to CTRL slices (Figure 6B–D). These results suggest that NMD modulates spontaneous Ca²⁺ activity in mouse astrocytes and are consistent with an enrichment of Ca²⁺ signaling associated pathways in NMD-deficient astrocytes (Figure 5F).

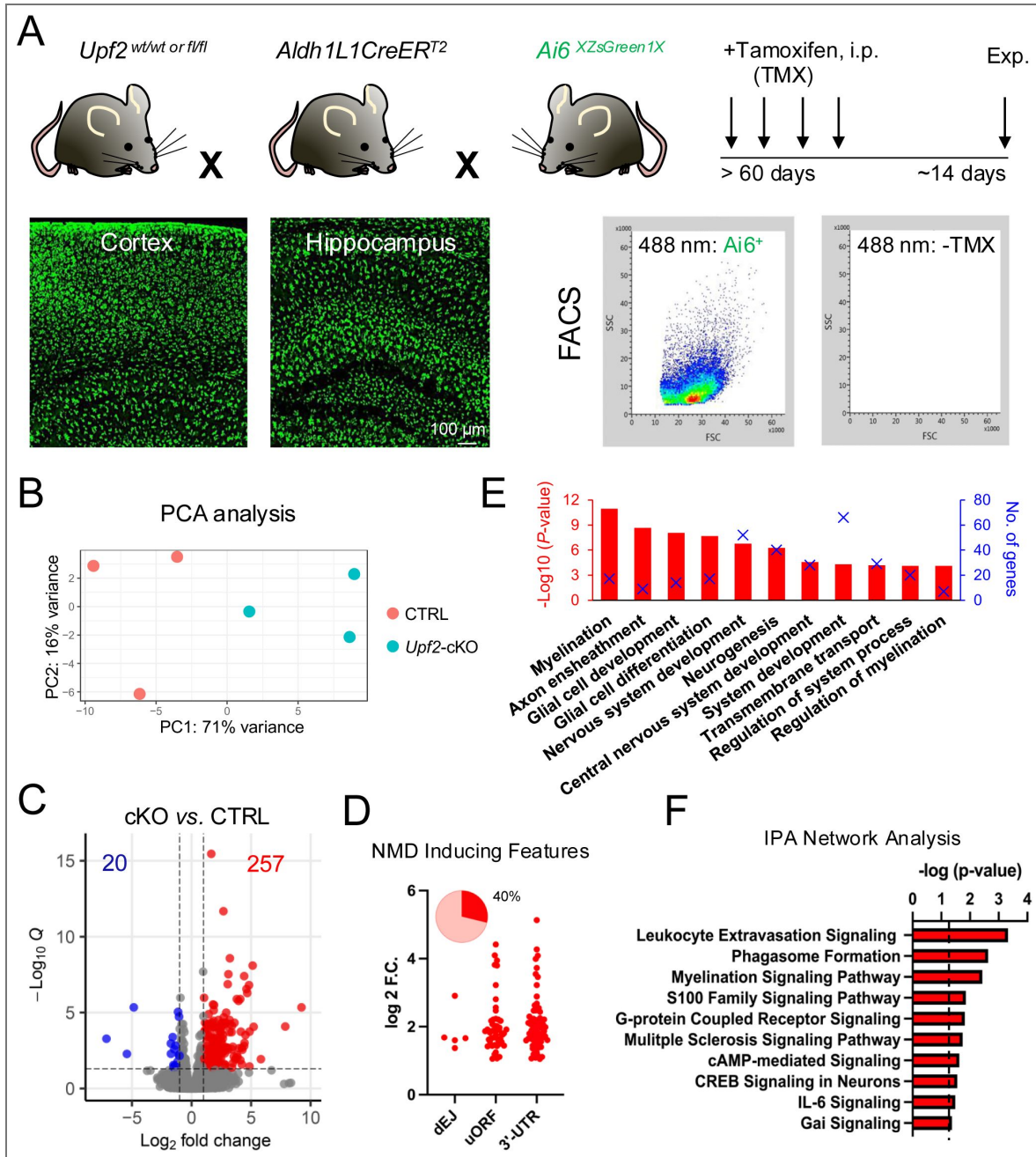


Figure 5. Identifying the physiological astrocytic targets of NMD *in vivo*.

(A) *Upf2* wt/wt or fl/fl mice were crossed with the *Aldh1L1CreERT2* and *Ai6-ZsGreen1* transgenic lines to select CTRL and cKO astrocytes with 488 nm fluorescence after tamoxifen dosing using FACS. Representative image demonstrating ZsGreen1 expression in cortical and hippocampal astrocytes (bottom, left). Side scatter (SSC) and forward scatter (FSC) plot for 488 nm fluorescence selection of ZsGreen1⁺ astrocytes and tamoxifen negative (-TMX) cell suspension showing no 488 nm positivity (bottom, right). (B) Principal component analysis (PCA) of RNA-seq datasets from CTRL and cKO astrocytes, as defined in panel (A). (C) Differentially expressed genes (DEGs; $q < 0.05$, fold change > 2) identified from the RNA-seq analysis of CTRL and cKO astrocytes in panel (B). (D) Upregulated DEGs containing at least one NMD inducing feature: downstream Exon-Junction complex-dEJ, upstream Open Reading Frame-uORF, and long 3'-untranslated region-UTR length (>1500 nt). (E) Top biological functions associated with upregulated genes defined in panel (C). Statistical significance [$-\log_{10}(p\text{-value})$] is indicated by the bar (bottom). The number of DEGs for a given category is indicated by an "X" (top). (F) Ingenuity Pathway Analysis (IPA) of upregulated genes defined in panel (C). Statistical significance [$-\log_{10}(p\text{-value})$] is indicated by the bar (top), with a p -value < 0.05 as the cut off. This figure, for the first-time, reveals the physiological astrocytic transcripts regulated by NMD *in vivo* and their associated biological pathways.

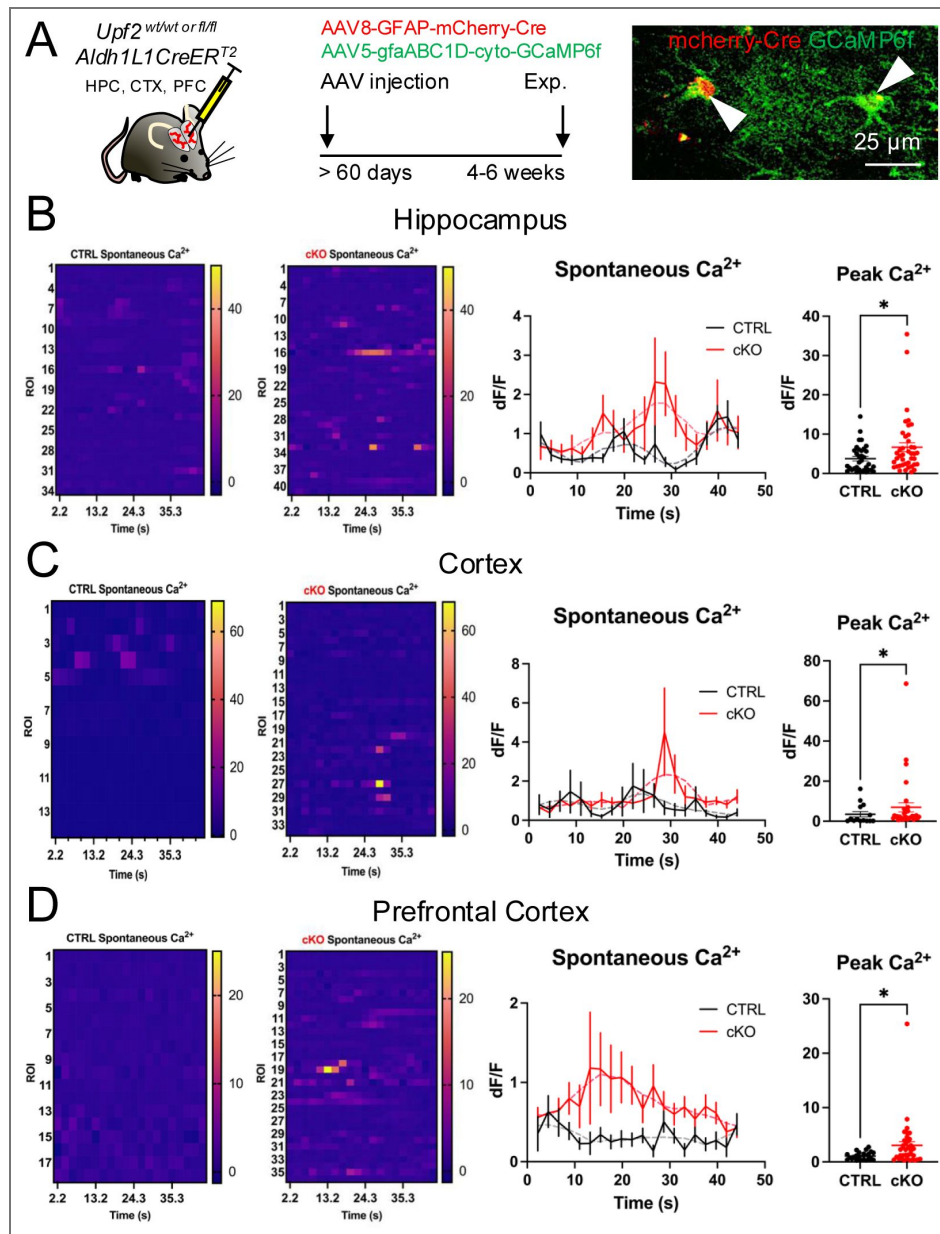


Figure 6. NMD-deficient astrocytes exhibit altered Ca^{2+} activity.

(A) Schematic of adeno-associated viral delivery of AAV8-GFAP-mCherry-Cre/AAV5-GfaABC1D-GCaMP6f reporters to hippocampus, visual cortex, and prefrontal cortex. Representative image of mCherry/GCaMP6f expression in region of interest-ROI. In all panels of this figure: heat map of spontaneous Ca^{2+} activity in CTRL and cKO conditions (left), temporal Ca^{2+} dynamic traces (middle), and peak Ca^{2+} summary data (right). (B) *Upf2* mutant astrocytes in hippocampus show elevated peak Ca^{2+} transients of spontaneous activity in comparison to CTRL (CTRL: 3.8 ± 0.6 , 34 ROIs, $n = 6$ mice; cKO: 6.7 ± 1.1 , 41 ROIs, $n = 8$ mice, $p = 0.038$, Mann-Whitney test). (C) *Upf2* deficient astrocytes in visual cortex exhibit enhanced peak Ca^{2+} transients of spontaneous activity as compared to CTRL (CTRL: 3.5 ± 1.3 , 14 ROIs, $n = 4$ mice; cKO: 6.9 ± 2.2 , 34 ROIs, $n = 5$ mice, $p = 0.046$, Mann-Whitney test). (D) *Upf2* cKO astrocytes in prefrontal cortex display increased peak Ca^{2+} transients of spontaneous activity as compared to CTRL (CTRL: 1.1 ± 0.1 , 22 ROIs, $n = 4$ mice; cKO: 3.0 ± 0.7 , 36 ROIs, $n = 5$ mice, $p = 0.013$, Mann-Whitney test). Data are presented as mean \pm S.E.M. * denotes $p < 0.05$. This figure highlights that UPF2-NMD deficient astrocytes exhibit elevated Ca^{2+} transients in hippocampus, visual cortex, and prefrontal cortex.

Preventing abnormally high basal Ca²⁺ activity in NMD-deficient astrocytes restores normal excitatory synapse function and behavior in *Upf2*-cKO mice

Astrocytes respond to neuronal activity by elevating their cytosolic Ca²⁺ concentrations (73, 77), which, in turn, feedback to regulate synaptic transmission strength (3–5). Consistent with this, astrocytic Ca²⁺ activity has been linked to various cognitive processes and abnormal animal behaviors (74, 78–81). This led us to hypothesize that the exaggerated Ca²⁺ activity in NMD-deficient astrocytes is responsible for altering synaptic function and thus mouse behavior. To test this, we performed a rescue experiment. We took advantage of the AAV5-GfaABC1D-hcPW2 virus carrying a Ca²⁺ extrusion (CalEx) pump shown to reduce Ca²⁺ levels in astrocytes (79, 80). We first determined whether the CalEx pump could decrease spontaneous Ca²⁺ activity in NMD-deficient astrocytes. Using stereotaxic surgeries, we injected CalEx, mCherry-Cre, and cyto-GCaMP6f viruses to hippocampus, visual cortex, and prefrontal cortex (Figure 7A). Our calcium imaging analysis revealed that the AAV5-GfaABC1D-hcPW2 virus lowered spontaneous peak Ca²⁺ transients in *Upf2*-cKO astrocytes to CTRL levels across all brain areas tested (Figure 7B). We next asked if reducing Ca²⁺ to CTRL levels in *Upf2*-cKO mice was sufficient to reverse defects in these NMD-deficient mice. To do this, we generated CTRL + CalEx and cKO + CalEx conditions while CTRL and cKO groups received no CalEx (Figure 7C). Across all test groups, we targeted viral delivery to hippocampus, visual cortex, and prefrontal cortex. To determine rescue effects, we first assessed PSD-95 density and synaptic function. Modulation of Ca²⁺ activity in *Upf2* cKO astrocytes did not restore PSD-95 density to CTRL levels (Figure 7D) however an upward trend was notable, raising the possibility that basal neurotransmission could be elevated. Consistent with this, CalEx manipulation shifted synaptic strength towards CTRL values in cKO acute hippocampal slices (Figure 7E). We also tested the cKO + CalEx mice for the observed anxiety-like phenotype (Figure 7F). As in the previous experiments (Figure 4B), cKO mice exhibited less time in the open arms compared to CTRL mice in the EPM in these rescue experiments, confirming an anxiety-like phenotype (Figure 7F). However, cKO mice manipulated with CalEx performed similarly to CTRL mice in the EPM indicating rescue of anxiety-like behavior in these animals (Figure 7F). Taken together, these results suggest that increased Ca²⁺ activity in NMD-deficient astrocytes is responsible for disrupting basal neurotransmission and Ca²⁺ modulation can correct synaptic strength and anxiety phenotypes in *Upf2* cKO mice.

Discussion

Despite being well established that astrocytes perform several critical functions in the brain, the molecular mechanisms governing astrocyte activity are poorly understood. Intracellular Ca²⁺ has been widely accepted to play a vital role in encoding and transmitting information within astrocytes and thereby regulating many functions of these cells. However, molecular programs regulating astrocytic Ca²⁺ dynamics remain to be fully identified. Here, we identified the RNA degradation pathway, NMD, as a key brake that prevents abnormally high basal Ca²⁺ activity in astrocytes. Our results highlight that astrocytic RNA degradation plays a crucial role in maintaining neuro-glia interactions that support proper brain function.

RNA regulation in higher brain function has been mostly studied at the level of RNA translation in neurons. Only in the last decade neuronal RNA degradation has been recognized as a regulator of spatiotemporal gene expression to support synaptic plasticity and cognitive function. Therefore, one of the most intriguing aspects of our findings is providing evidence that astrocytic RNA degradation, similar to neuronal RNA degradation, also contributes to regulation of synaptic function and behavior via neuro-glia interactions.

Our study has revealed that NMD is required in astrocytes to sustain their size. Astrocyte's unique morphology and interactions with synapses play a crucial role in regulating and maintaining synaptic plasticity (82, 83). Across brain structures, we observed volume and surface area was

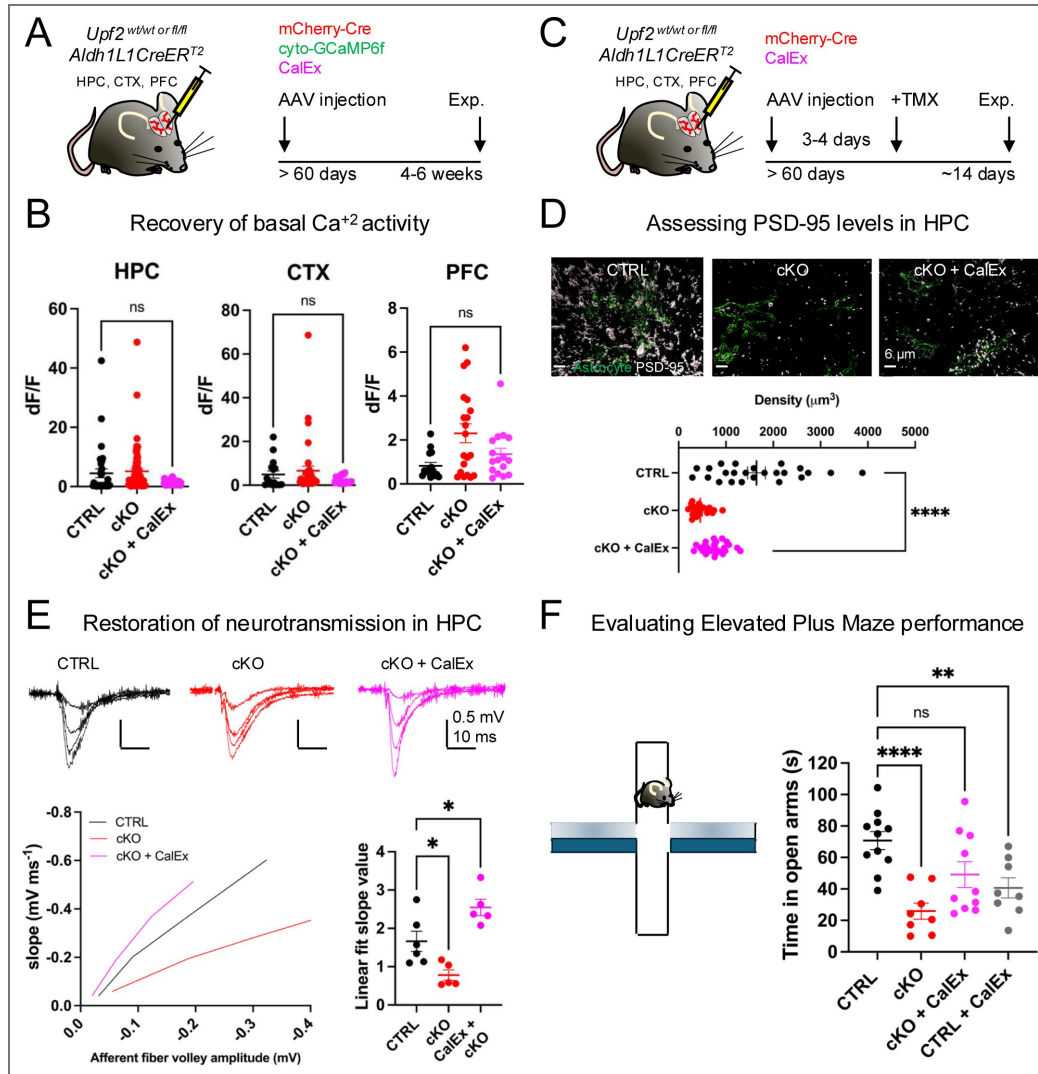


Figure 7. CalEx restores basal Ca²⁺ activity in *Upf2* cKO astrocytes and rescues neurotransmission along with anxiety.

(A) Scheme for viral delivery and timeline for Ca²⁺ measurement experiments. (B) CalEx diminished Ca²⁺ events to CTRL levels in hippocampus (CTRL: 4.5 ± 1.5, n = 6 mice, 32 ROIs; cKO: 5.1 ± 0.9, n = 8 mice, 68 ROIs; cKO + CalEx: 1.4 ± 0.1, n = 4 mice, 46 ROIs; One-way ANOVA DF = 2, F = 4.802, p = 0.0096, post-hoc Tukey's multiple comparisons test CTRL vs. cKO + CalEx, p = 0.096). CalEx Ca²⁺ events are comparable to CTRL in visual cortex (CTRL: 4.9 ± 1.7, n = 4 mice, 16 ROIs; cKO: 6.6 ± 2.1, n = 6 mice, 36 ROIs; cKO + CalEx: 2.3 ± 0.4, n = 4 mice, 19 ROIs; One-way ANOVA DF = 2, F = 1.261, p = 0.29). CalEx prefrontal cortex Ca²⁺ events are similar to CTRL (CTRL: 0.8 ± 0.2, n = 4 mice, 15 ROIs; cKO: 2.3 ± 0.4, n = 4 mice, 20 ROIs; One-way ANOVA DF = 2, F = 5.165, p = 0.0093, post-hoc Tukey's multiple comparisons test CTRL vs. cKO + CalEx, p = 0.542). (C) Scheme for viral delivery and tamoxifen treatment followed by rescue assays for PSD-95 density, neurotransmission, and animal behavior. (D) Total PSD-95 density is not restored to CTRL levels by CalEx manipulation in *Upf2* cKO mice (CTRL: 1648 ± 188, n = 24 ROIs, 4 mice; cKO: 459 ± 41, n = 21 ROIs, 4 mice; cKO + CalEx: 771 ± 52, n = 24 ROIs, 4 mice; One-way ANOVA DF = 2, F = 10.28, p < 0.0001, post-hoc Tukey's multiple comparisons test CTRL vs. cKO + CalEx, p < 0.0001). (E) CalEx elevates synaptic strength in hippocampus of *Upf2* cKO mice as compared to CTRL (CTRL: Linear fit 1.88 ± 0.1, r = 0.99, n = 6 slices, 3 mice; cKO: Linear fit 0.84 ± 0.05, r = 0.99, n = 5 slices, 4 mice; cKO + CalEx: Linear fit 2.66 ± 0.24, r = 0.98, n = 5 slices, 3 mice. One-way ANOVA DF = 2, F = 15.08, p = 0.0004, post-hoc Tukey's multiple comparisons test CTRL vs. cKO + CalEx, p = 0.033). (F) CalEx increases elevated plus maze open arm time in *Upf2* cKO mice (CTRL: 70.7 ± 5.7, n = 11 mice; cKO: 25.9 ± 5.2, n = 8 mice; cKO + CalEx: 49.1 ± 8.1, n = 10 mice; CTRL + CalEx: 40.6 ± 6.4, n = 8 mice, One-way ANOVA DF = 3, F = 8.24, p = 0.0003, post-hoc Tukey's multiple comparisons test CTRL vs. cKO + CalEx, p = 0.086). Data are presented as mean ± S.E.M. * denotes p < 0.05, ** denotes p < 0.01, **** denotes p < 0.0001, ns = not significant. This figure depicts that restoring Ca²⁺ levels in astrocytes of *Upf2* cKO mice recovers basal neurotransmission and minimizes anxiety-like behavior.

significantly reduced in NMD-deficient astrocytes (Figure 1 [↗](#)). This is consistent with the finding that several putative NMD-target transcripts encode proteins involved in cell size regulation and/or morphology (see below).

Given that a single mouse astrocyte can interact with ~100,000 synapses (1), alterations to astrocyte cytoarchitecture have been reported to destabilize neuro-glia interactions. Indeed, we found that PSD-95 density of excitatory neurons is decreased across brain areas in cKO mice (Figure 2 [↗](#)). This phenotype was accompanied with dampened engulfment of synaptic material in the same regions (Figure 2 [↗](#)). Concomitantly, dendritic spine density was reduced in CA1 pyramidal neurons of the hippocampus (Figure 2 [↗](#)). In line with the depletion of synapse density, electrophysiological measurements revealed a decline in synaptic strength (Figure 3 [↗](#)). These findings support a model that by regulating astrocytic remodeling, NMD supports synaptic architecture, leading to proper synapse density and strength. A non-mutually exclusive possibility is that NMD modulates astrocytic phagocytic activity whose disruption leads to reductions in synapse density and overall strength. Temporal examination of these cellular adaptations may aid to disambiguate cooperative or specific spatiotemporal effects on synapse structure-function resulting from NMD disruption in astrocytes.

We also identified astrocytic NMD as a regulator of synaptic plasticity. *Upf2*-cKO mice demonstrated a lack of synaptic potentiation in response to physiological patterns of neural activity that trigger LTP (Figure 3 [↗](#)). Recently, astrocyte remodeling of perisynaptic processes was shown to impact LTP magnitude (82), highlighting the critical role of neuro-glia structural modifications in synaptic function (83–85). Intriguingly, previous studies have shown that astrocytic S100B protein and interleukin-6 (IL-6) manipulations can downregulate LTP magnitude (86, 87) and these biological pathways were identified in our bioinformatic analysis (Figure 5F [↗](#)). Recent evidence suggests that NMD-target mRNAs differ across cell types (ie. embryonic vs. neural progenitor cells) and may display brain-region specificity (31). Additionally, NMD target mRNAs have been mostly identified in neural stem cells and neurons in previous studies. Thus, to gain mechanistic insight into the functions of NMD in astrocytes, it is critical to identify NMD targets in these cells. We accomplished this by combining conditional deletion of *Upf2* and next-generation RNA sequencing. Consistent with the RNA degradation function of NMD, more than 90% of DEGs exhibited upregulation upon disruption of NMD in astrocytes. Indirect NMD targets, likely together with the direct targets with non-canonical- yet to be identified- NMD-inducing features, could comprise the remaining 60%. We found that NMD regulates specific mRNAs that exhibit critical functions in astrocyte cytoarchitecture and Ca^{2+} signaling in astrocytes. For example, *S100b* is implicated in astrocyte shape and migration (88). We identified *S100b* as an upregulated DEG that did not carry a canonical-NMD inducing feature. Intriguingly, the release of S100b protein can influence direct or indirect phagocytic activity by inducing proinflammatory pathways that could remodel neuro-glia interactions (89). This is consistent with upregulation of transcripts linked to S100 Family signaling pathway and IL-6 signaling in *Upf2* cKO astrocytes. Similarly, *Cldn9*, *Cldn11*, and *Mmp8* are upregulated DEGs suggested to mediate morphological adaptations in various conditions (90–92). Among them, *Cldn9* contains a uORF and has the potential to be directly targeted by NMD. Meanwhile, *Gabbr2*, encoding for GABAB, and *Adora1*, encoding for A1 receptor, stand out as GPCRs implicated in downstream Ca^{2+} signaling effector pathways that could influence neuro-glia communication. Notably, both *Gabbr2* and *Adora1* were detected as upregulated candidates containing canonical NMD-inducing features.

Here, we report evidence that NMD functions to suppress basal Ca^{2+} activity in astrocytes. Our findings provide empirical evidence that it is critical that NMD suppress basal Ca^{2+} activity in astrocytes, as otherwise this leads to alterations in synaptic strength (Figure 7E [↗](#)) and promotes anxiety in mice (Figure 7F [↗](#)). This is consistent with the known role of Ca^{2+} in astrocytes (58, 64, 74, 78–81). For example, abnormally high basal Ca^{2+} levels could lead to dysregulated release of gliotransmitters (e.g., ATP or glutamate) and other glia-derived molecules known to modulate neural excitability and synaptic transmission (4, 6, 93, 94). This would explain why we observed a

decline in synaptic strength and limited synaptic plasticity in NMD-deficient *Upf2*-cKO mice. Previous studies have also suggested that astrocytic GABAB and A1 receptor signaling pathways contribute to Ca^{2+} fluctuations and modulate excitatory transmission, respectively (95–97). Ultimately, maladaptive astrocyte Ca^{2+} influx may impact neural circuit function leading to alterations in animal behavior. We provide evidence that astrocytic NMD is required to restrain anxiety in adulthood. In fact, astrocytes in different brain regions have been reported to suppress anxiety-like behavior (58, 78, 98–100) and astrocytic Ca^{2+} has been linked to anxiety (58). Specifically, extruding Ca^{2+} from nucleus accumbens astrocytes by overexpression of the CalEx pump led to pronounced reductions in anxiety behavior and increased exploratory behavior in mice (99). In contrast, mice with chronically activated Ca^{2+} signals in ventral CA1 exhibited enhanced anxiety behavior (100). Our study identifies astrocytic NMD as a mechanism that suppresses anxiety by modulating basal Ca^{2+} activity in astrocytes. We have previously reported that neuronal NMD has major roles in cognitive function influencing various types of learning and different aspects of memory (23). Our current study determined that NMD in astrocytes specifically contributes to regulation of anxiety, suggesting a complementary cell-specific role for this molecular program in behavior.

In conclusion, our findings provide key insights into constructing a comprehensive model of how cell-specific mRNA degradation impacts synaptic function and animal behavior. Our studies also have broad relevance for understanding the significance of astrocytic mechanisms in synaptic plasticity, disruption of which contributes to several brain ailments. Here, we specifically disturbed NMD in astrocytes, which allowed us to evaluate the physiological roles of this highly conserved and selective RNA turnover pathway in astrocyte biology and synaptic function. However, astrocytes exhibit regional and functional heterogeneity (101, 102). While our work establishes the physiological requirement for astrocytic NMD in three critical brain regions, future studies are required to define the spatiotemporal impact of NMD on astrocyte-neuron function in the nervous system.

Materials and methods

Transgenic Animals and Tamoxifen Dosing

Animal handling followed an approved protocol by the Institutional Animal Care and Use Committees of Weill Cornell Medicine and the Albert Einstein College of Medicine in accordance with NIH guidelines. The *Upf2* conditional knockout mouse line (41) was backcrossed for at least eight generations with C57BL/6J (Stock#: 000664, The Jackson Laboratory) mice to generate *Upf2*^{wt/wt} and *Upf2*^{fl/fl} animals that were bred with *Aldh1L1CreER*^{T2} (B6N.FVB-Tg(Aldh111-Cre/ERT2)1Khakh/J Stock#: 031008, The Jackson Laboratory (42)) transgenic mice to enable CRE expression in astrocytes of *Upf2*^{wt/wt} and *Upf2*^{fl/fl} mice in a tamoxifen dependent manner. Mice were housed in 12:12 light-dark conditions with *ad libitum* feed diet. At 2–4 months of age *Upf2*^{wt/wt}:*Aldh1L1CreER*^{T2} (CTRL) and *Upf2*^{fl/fl}:*Aldh1L1CreER*^{T2} (cKO) mice received intraperitoneal tamoxifen (T5648, Sigma-Aldrich, USA) in corn oil at 200 mg/kg for 4 consecutive days using a 26 gauge Sub-Q syringe (309597, Becton Dickinson & Co., USA). For fluorescence expression of the ZsGreen1 reporter, the Ai6 transgenic mouse line was implemented (B6.Cg-Gt(ROSA)26Sortm6(CAG-ZsGreen1)Hze/K, Stock#: 007906, The Jackson Laboratory (103)). *Upf2*^{wt/wt}:*Aldh1L1CreER*^{T2}:Ai6 (CTRL) and *Upf2*^{fl/fl}:*Aldh1L1CreER*^{T2}:Ai6 (cKO) followed the previously mentioned tamoxifen regime. Experimental manipulations were initiated 12–14 days after the last day of tamoxifen dosing. Male and female mice were included for all experimental manipulations.

Perfusion and Cryo-sectioning

Mice were anesthetized using 4% isoflurane (11695-6777-2, Covetrus) and intracardially perfused with 10 mL of 1X phosphate buffer saline-PBS (MRGF-6235-020Q, GrowCells) to flush blood, followed by ~15 mL of 4% paraformaldehyde-PFA (15713-S, Electron Microscopy Sciences) for fixation. Following PFA perfusion, mouse brains were extracted and stored in 4% PFA at 4°C

overnight. Next day, brains were rinsed with PBS and stored at 4°C in 30% sucrose (S0389, Sigma Aldrich). After achieving sucrose penetration for cryoprotection, brains were embedded in tissue trays containing OCT compound (4583, Sakara), frozen on dry ice, and stored at -80 °C until cryosectioning. A Leica CM3050S cryostat enabled the collection of frozen sections (25-70 µm thickness) mounted onto microscope slides and stored at -20 °C for downstream application.

Immunohistochemistry and Confocal microscopy

Frozen sections were rehydrated using PBS and subsequently rinsed 3 x for 5 min on a rotating tray, 45 rpm. Tissue slides were then permeabilized and blocked with a PBS solution containing 0.2-0.5% Triton-X (X100, Sigma Aldrich) and 10% normal goat serum (G9023, Sigma Aldrich) for 1 h. After permeabilization and blocking, tissue slides were incubated at 4°C overnight with primary antibodies at specified dilutions, unless stated otherwise. Next day, tissue slides were washed with PBS 3 x for 15 min on a rotating tray, 45 rpm. Secondary antibodies were added and incubated at room temperature for 1-2 h, at specified dilutions, unless stated otherwise. In some cases, tissue slides were rinsed with PBS and incubated with Hoechst 33342 (H3570, ThermoFisher Sci) for 5 min. After 3 x 10 min PBS washes, tissue slides were allowed to air dry protected from light. ProLong Anti-Fade Glass Mountant (P36980, ThermoFisher Sci) was added, coverslips adhered, and slides were stored at 4°C. When recommended, antigen retrieval was performed by incubating tissue slides in citrate buffer, pH = 6 (C9999, Sigma Aldrich) and heated until solution boiled. The following primary and secondary antibodies were used: rabbit anti-hUPF2 1:500 (Jens Lykke-Andersen Lab), chicken anti-GFAP 1:5000 (PA1-10004, ThermoFisher Sci), chicken anti-Iba1 1:500 (234009, Synaptic Systems), rat anti-Mbp 1:1000 (ab7349, 1 h primary incubation, Abcam), mouse anti-PSD-95 1:500 (MA1-046, ThermoFisher Sci), rat anti-LAMP2 1:300 (ab13524, Abcam), guinea pig anti-S100B 1:200 (287004, Synaptic Systems), chicken anti-GFP 1:100 (A10262, ThermoFisher Sci), mouse anti-GFP 1:50 (A11120, ThermoFisher Sci), rat anti-mCherry 1:50 (M11217, ThermoFisher Sci), anti-rabbit Alexa Fluor 488 1:500 (A32731, ThermoFisher Sci), anti-chicken Alexa Fluor 647 1:1000-GFAP, 1:500-Iba1 (A21449, ThermoFisher Sci), anti-rat Alexa Fluor 546 1:500 (A11081, 1 h secondary incubation, ThermoFisher Sci), anti-mouse Alexa Fluor 546 1:500 (A11003, ThermoFisher Sci), anti-rat Alexa Fluor 633 1:500 (A2104, ThermoFisher Sci), anti-guinea pig Alexa Fluor 546 1:500 (A11074, Thermo Fisher Sci), anti-chicken Alexa Fluor 488 1:500 (A11039, ThermoFisher Sci), anti-mouse Alexa Fluor 488 1:500 (A21131, Thermo FisherSci), anti-rat FITC 1:500 (11-4817-82, ThermoFisher Sci), Hoechst 334222 1:5000 (H3570, ThermoFisher Sci). An Olympus Fluoview FV1000 confocal microscope enabled the acquisition of fluorescence images at 512 x 512 or 640 x 640 pixel resolution assisted with Olympus Fluoview 4.2 software. The spinning-disk confocal Andor DragonFly microscope using 1024 x 1024 pixel resolution operated with Fusion software also assisted image acquisition. Laser channel detections were set to 405 nm, 488 nm, 546 nm, and 647 nm for image acquisition using 10X (dry), or 60X (1.4 NA) oil-immersion objective with manufacturer oil (Olympus Immoil F30CC, Type-F). Images were processed in Fiji of at least four field of views per genotype.

Fluorescence Assisted Cell Sorting

To isolate 488 nm⁺ astrocytes, *Upf2*^{wt/wt};*Aldh1L1CreER*^{T2} and *Upf2*^{fl/fl};*Aldh1L1CreER*^{T2} mice were crossed with the Ai6 reporter line from The Jackson Laboratory to generate triple transgenic mice. Fluorescence Assisted Cell Sorting (FACS) was performed ~14 days after the last day of tamoxifen dosing. Mice were anesthetized with 4% isoflurane followed by intracardial perfusion using Hanks' Balanced Salt Solution (88284, ThermoFisher Sci) to flush blood. Next, brains were extracted onto ice-cold petri dishes for cortex-hippocampus dissections. Cortical-hippocampal samples from each genotype were collected in ice-cold petri dishes containing DNase, RNase, protease free PBS (BP24384, Fisher Sci). After tissue collection (n = 3 brains/genotype), samples were manually chopped using a sterile scalpel. Cell dissociation was performed using a Papain Dissociation Kit (LK003150, Worthington Biochemical Corp). During the papain dissociation step, RNase murine inhibitor (M0314S, New England Biolabs) was added at 1U/µL working concentration. Digested cell suspensions were passed through a 40 µm nylon mesh cell strainer (431750, Corning) followed by cell centrifugation at 300 g for 5 min. Cell pellets were gently

resuspended and layered onto an ovomucoid gradient for final cell pelleting at 70 g for 6 min. CTRL and cKO cell pellets were re-suspended in 0.5% BSA (0332, VWR Chemicals) made in PBS solution for myelin removal using a magnetic bead kit (130-096-733, Miltenyi Biotec) with LS columns (130-042-401, Miltenyi Biotec). After myelin depletion, CTRL and cKO cell collections were brought to a cell sorter. A BD Influx system enabled FACS and an Ai6 negative cell suspension served as a negative control. Forward and side scattering gates were used to remove clumps of cells and debris. On average a total of $1\text{--}1.6 \times 10^6$ purified cells per genotype were collected in 0.5% BSA-PBS containing RNase murine inhibitor for downstream RNA extraction.

RNA Sequencing and Analysis

CTRL and cKO cell samples purified by FACS from 6 mice per genotype (with 2 technical replicates) were immediately processed for RNA extraction using the RNeasy Mini plus kit (74136, Qiagen). After following the manufacturer's specifications, RNA quantity and quality was assessed using Agilent Bioanalyzer Tape station and picogel analyses. RNA integrity number (RIN) values ranging from 7.0 – 9.0 for CTRL and cKO RNA samples were used to prepare the library using the IlluminaNextSeq500 SMART-Nextera kit, as per manufacturer's instructions. Libraries were sequenced (pair-end reads) with an Illumina NextSeq 500 platform for 50 cycles, with a depth of 40M reads per sample.

As performed previously (22, 104), reads were filtered for quality and aligned with STAR (2.5.2b) against the GRCm39 (Ensembl version 105). The exon counts were aggregated for each gene to build a read count table using SubRead function featureCounts. Differentially expressed genes were defined using the DESeq2 program with the following thresholds: $|\text{Log}_2\text{FC}| > 1$ and $q\text{-val} < 0.02$. The database for annotation, visualization and integrated discovery (DAVID) v6.8 was used for GO analysis. For pathway analysis, the upregulated genes, along with their fold-change and adjusted p -values were uploaded to Ingenuity Pathway Analysis (Qiagen) and analyzed. A p -value < 0.05 was used as the significance threshold, and the enriched signaling pathways were categorized based on z-score values to generate predicted biological pathways.

To identify NMD-inducing features among upregulated transcripts, only Ensembl transcripts with detectable 5'UTRs and 3'UTRs were considered. Transcripts were classified as having a dEJC if they contained at least one exon-exon junction ≥ 50 nucleotides downstream of the stop codon defining the main ORF. Transcripts were considered to have an "upstream (u) ORF" if it included an ORF upstream of the main ORF that was ≥ 30 nucleotides in length and initiated by a codon in a context with a purine at the -3 position or a guanine at the $+1$ position (relative to the A in the AUG initiation codon $[+1]$). To minimize the identification of uORFs capable of reinitiating translation (and thereby escaping NMD), we required that the uORF not overlap with any sequence in the main ORF.

Astrocyte Imaris 3D reconstructions, PSD-95 density, and synapse engulfment assay

For Lck-GFP astrocyte morphology, 70 μm -thick frozen brain sections from both genotypes were immunostained with mouse anti-GFP 1:50 (A11120, ThermoFisher Sci) and rat anti-mCherry 1:50 (M11217, ThermoFisher Sci) antibodies. For synapse density and engulfment assays, 50 μm -thick frozen brain sections from both genotypes were immunostained with anti-PSD95 and anti-LAMP2 antibodies. Fluorescence imaging was carried out on an inverted Leica DMi8 microscope equipped with Andor Dragonfly 200 unit (405 nm, 488 nm, 561 nm, 640 nm and 730 nm lasers) operated by Fusion software. For each mouse, three to six ROIs per brain region (HPC, CTX, and PFC) were acquired (30 μm depth scan size, 0.2 μm interval Z-stack, with 63X objective and 1024 x 1024 pixel resolution). 3D-surface rendering and quantification of cell volume and engulfed materials were carried out blinded using the Imaris 10.2.0 software. PSD-95 puncta colocalized with LAMP2 puncta within cells were considered as engulfed material determined by implementing the "mask" function of Imaris as previously described (105, 106). To normalize the engulfed material, we divided the volume of engulfed PSD-95 by the volume of the cell. From cell volume measurements the radius was utilized to calculate surface area across brain regions.

Stereotaxic Surgeries

Transgenic mice were anesthetized using 4% isoflurane mixed with O₂ flowing at 2 mL/min. Mice were placed in a Kopf stereotaxic instrument and anesthesia was sustained at 1.5-2% isoflurane-O₂ mix. For spine density experiments, 100-200 nL of AAV5-CamKII α -EGFP (50469, Addgene) was delivered bilaterally using a Hamilton syringe at stereotaxic coordinates targeting the CA1 area of the hippocampus (A/P: -2.0, M/L: 1.5, D/V: -1.1 mm). Animals were allowed to recover from surgery for three days and then received tamoxifen administration. For astrocyte morphology experiments, 300-500 nL of AAV8-GFAP-mCherry-Cre (UNC Vector Core) and AAV5-GfaABC1D.PI.Lck-GFP.SV40 (105598, Addgene) mixed at a (1:2 ratio) was delivered at stereotaxic coordinates targeting prefrontal cortex (A/P: +1.8, M/L: 0.3, D/V: -1.6 mm), the CA1 area of the hippocampus (A/P: -2.0, M/L: 1.5, D/V: -1.2 mm) and visual cortex (A/P: -2.0, M/L: 1.5, D/V: -0.75 mm). After recovering from surgery, (3-4 days) animals underwent tamoxifen administration. For astrocyte calcium imaging experiments, 1.2 μ L of AAV8-GFAP-mCherry-Cre (UNC Vector Core) and AAV5-gfaABC1D-cyto-GCaMP6f (52925, Addgene) mixed at a (1:2 ratio) was delivered to prefrontal cortex, hippocampus, and visual cortex using the previously mentioned stereotaxic coordinates. Two-photon imaging experiments were performed 4-6 weeks post-surgery. For CalEx calcium imaging 1.5 μ L of AAV5-GfaABC1D-mcherry-hPMCA2w/b (111568, Addgene) virus together with AAV5-gfABC1D-cyto-GCaMP and AAV8-GFAP-mCherry-Cre mixed at a (3:2:1 ratio) was injected at the stereotaxic coordinates previously described and experiments were performed 4-6 weeks post-surgery. For CalEx behavioral rescue experiments 1.5 μ L of AAV5-GfaABC1D-mcherry-hPMCA2w/b and AAV8-GFAP-mCherry-Cre mixed at a (2:1 ratio) was delivered to prefrontal cortex, hippocampus, and visual cortex. Animals recovered from surgery for 3-4 days and underwent tamoxifen administration. All mice received meloxicam and bupivacaine following the IACUC recommendations of Weill Cornell Medicine. The EGFP, GCaMP6f and CalEx viruses were acquired from Addgene, the mCherry-Cre virus was ordered from the UNC Vector Core, Chapel Hill.

Spine Density Assessment

Transgenic mice were monitored for 72 h post-stereotaxic surgery and then dosed with tamoxifen. After ~14 days of the last tamoxifen dose, mice were anesthetized with 4% isoflurane and intracardially perfused with PBS to flush blood followed by 4% PFA. Brains were fixed in 4% PFA overnight and then cryoprotected with 30% sucrose. Upon achieving cryoprotection, brains were embedded in tissue trays, frozen in OCT compound, and stored at -80°C. Coronal hippocampal sections of 250-300 μ m thickness were mounted onto microscope slides using a Leica CM3050S cryostat and stored at -20°C. Next day, coronal sections underwent immunostaining procedures to enhance EGFP signal with an anti-GFP chicken antibody 1:50 (A10262, ThermoFisher Sci) or mouse anti-GFP 1:50 (A11120, ThermoFisher Sci). In some cases, tissue slides were incubated with Hoechst 33342 1:5000 (H3570, ThermoFisher Sci) for 5 min then washed with PBS 3 \times 5 min, to visualize brain cells. After following the immunostaining procedures previously described, tissue slides were allowed to air dry protected from light and Pro-Long Antifade Glass Mountant was added for coverslip adhesion. The Olympus Fluoview FV1000 confocal microscope enabled the acquisition of EGFP signals at 640 x 640 pixel resolution using the 488 nm laser wavelength path with a 60X (1.4 NA, Nikon) oil-immersion objective at 4.0 μ s/pixel, digital zoom 8X. Z-stack images of 10-15 μ m thickness with 0.2 μ m steps were acquired from dendrites of hippocampal CA1 pyramidal neurons at least 150 μ m away from the cell body. Images were processed in Fiji for Z-projections of at least 5 field of views per sample/genotype. Spine structures were quantified in 10 μ m bins per dendritic image to determine spine density in CTRL and cKO conditions in a blinded manner.

Hippocampal slice preparation

Male and female mice were anesthetized with 4% isoflurane followed by perfusion with 25 mL of cold NMDG solution containing in (mM): 93 NMDG, 2.5 KCl, 1.25 NaH₂PO₄, 30 NaHCO₃, 20 HEPES, 25 glucose, 5 sodium ascorbate, 2 Thiourea, 3 sodium pyruvate, 10 MgCl₂, 0.5 CaCl₂, brought to pH 7.35 with HCl (SA49, Fisher Sci). Following perfusion, the brain was extracted and dissected

hippocampi were cut using a VT1200s (Leica Co.) microslicer in cold NMDG solution. Acute hippocampal slices (300-400 μm) were collected and placed in a chamber containing extracellular artificial cerebrospinal fluid (ACSF) recording solution containing (in mM): 124 NaCl, 2.5 KCl, 26 NaHCO_3 , 1 NaH_2PO_4 , 2.5 CaCl_2 , 1.3 MgSO_4 and 10 glucose. The slice chamber was warmed in a water-bath at 33-34°C. After 10 min of completing slice collection, the chamber was moved to room temperature and slices were allowed to recover for at least 45 min prior to experimentation. All solutions were equilibrated with 95% O_2 and 5% CO_2 (pH 7.4).

Electrophysiology

Electrophysiological experiments were performed at 31.2 ± 1 °C under temperature control (TC-344C, Warner Instruments) in a submersion-type recording chamber perfused at 2 mL/min with ACSF. A stimulating glass electrode was filled with ACSF and placed in *stratum radiatum* to activate Schaffer collateral inputs using a Isoflex stimulus isolator (A.M.P.I) with a 100 μs pulse width duration. Extracellular field excitatory postsynaptic potentials (fEPSPs) were recorded using a patch-type pipette filled with 1 M NaCl. For long-term potentiation (LTP) recordings, slices of 400 μm thickness were stimulated every 20 s for a baseline fEPSP period of 15 min. LTP was induced by theta-burst stimulation (TBS) consisting of: 10 bursts of 5 pulses at 100 Hz delivered every 200 ms (inter-burst interval) repeated 4X (every 5 s) as previously described (105). LTP experiments were carried out in the presence of picrotoxin (100 μM , P1675, Sigma Aldrich) and CGP-55845 (3 μM , No. 1248, Tocris Bioscience) to block inhibitory transmission. The last 10 min of fEPSP responses were compared to baseline average responses to determine the magnitude of potentiation. For extracellular field input-output and paired-pulse ratio experiments synaptic inputs were stimulated every 10 s. The stimulation intensity of an Isoflex stimulator was increased from 0-20 V in 5 V increments. Slopes of fEPSP responses and amplitudes of fiber volleys were determined using ClampFit 11.2 software. Paired-pulse ratio (PPR) was examined by delivering two stimuli at various inter-stimulus intervals (10-500 ms) and measuring the ratio of fEPSP slopes ($\text{fEPSP}_{\text{slope}2}/\text{fEPSP}_{\text{slope}1}$). Both input-output and paired-pulse ratio was performed in the absence of pharmacological drugs. Long-term depression (LTD) was induced using a low-frequency stimulation protocol (LFS: 900 pulses at 1 Hz). A 15 min baseline period was recorded prior to LTD induction and synaptic inputs were stimulated every 20 s. For chemical LTD, mGluR-LTD was elicited by bath-application of DHPG (50 μM , 5 min, No. 0342, Tocris Bioscience) after obtaining a 10 min baseline period. To determine the magnitude of depression for LFS and mGluR-LTD the last 10 min of fEPSP slope responses were compared to baseline averaged responses. Field recordings were registered with a MultiClamp 700B amplifier and AxonDigiData 1550B (Molecular Devices) and signals were filtered at 2 kHz and digitized at 5 kHz. Stimulation and acquisition were controlled with custom software (Igor Pro 6 or Clampex 11.2).

Two-photon laser scanning microscopy for astrocyte calcium imaging

Astrocyte calcium imaging experiments were conducted 4-6 weeks after stereotaxic surgery. An *In vitro* Ultima 2P microscope (Bruker Corp) with an Insight Deep See laser tuned to 780 nm was used to visualize mCherry-Cre⁺ signals at 512 x 512 pixel resolution across targeted brain areas with 6-8 mW laser power measured at the 60X objective (Nikon, 1.0 NA). Upon identification of mCherry-Cre⁺ regions of interest (ROI) the laser wavelength was tuned to 945 nm, 3-4 mW laser power, for detection of GCaMP6f signals. T-series (time-series) software (PrairieView 5.4, Burker Corp) captured spontaneous Ca^{2+} transients. Images from the time series were Z-projected to identify ROIs with standard deviations denoting Ca^{2+} fluctuations. The ROIs were analyzed in a semi-automated manner using Fiji. The average value of 3 frames was considered baseline fluorescence (F_0), and the corresponding change in fluorescence ($\Delta F = F - F_0/F_0$) was measured. Across ROIs, the highest $\Delta F/F$ at a given time point was determined as the peak Ca^{2+} amplitude analyzed in blind fashion.

Behavioral Paradigms

For all behavior experiments, animals were allowed to acclimate to room conditions for 1 h prior to initiating assays. Behavior rooms were monitored to maintain room temperature and humidity. Experimentation was conducted in 75% white light and 25% red light. Elevated plus maze was performed in 100% white light. Equipment underwent clidox sterilization between trials and 70% ethanol was used to clean contextual fear conditioning equipment. Male mice were tested prior to female mice.

Open Field

The open field assay was conducted using the SD instruments Open Field Equipment and software. A 16 x 16 beam array detected animal movement in X and Y coordinates. SD software calculated beam breaks for 12 interval phases of 5 min duration for a total trial period of 1 h. Total beam breaks was calculated by the sum of X and Y coordinates in 1 h.

Marble Burying

Standard home cages 27.5 cm (L) x 19.5 cm (W) x 15 cm (H) were filled with aspen chip bedding measuring a height of ~2 cm. Marbles arranged in a 5 x 4 (row x column) equidistant matrix assayed digging behavior. Each burying trial was 30 min in duration. Marbles covered by > 75% of aspen chip bedding met inclusion criteria for buried marbles.

Elevated Plus Maze

The Elevated plus maze apparatus was positioned and set for Noldus Ethovision XT software acquisition. Animals were tracked for an exploration trial period of 5 min. Open arm, center, and closed arm durations were calculated by Ethovision software. Our Plus Maze (San Diego Instruments) contains two open arms and two closed arms and relies upon the animal's natural tendency to stay in enclosed spaces and avoid open spaces and heights. Anxious animals will spend more time in the closed arms than less anxious animals, which will explore the open arms for a longer duration. EthoVision XT detects the center point, tail base, and nose point of the animal, allowing for accurate measurement of position and enabling us to discriminate between the subject only poking its nose around the corner or moving its entire body into one of the open arms of an elevated plus maze.

Contextual Fear Conditioning

Fear Conditioning chambers (Med Associates Inc.) comprise standard grid-floored chambers that are enclosed within a sound-attenuated cubicle. Each cubicle has its own lux-control box, standalone aversive stimulator, speaker (for conditioned-stimulus exposure) and high-speed firewire infrared video camera. The context of chambers can thus be modified to differ in lux, bedding (stored under grid-flooring), shape (by means of a Med Associates supplied insert) and smell (through use of a mild essence dilution added to the cleaning solution). Video scoring is automated, and occurs in real-time, by the proprietary Video Freeze (Med Associates Inc) software package, with freezing behavior programmed as a lack of movement detected across 30 frames (one second). On Day 1, animals underwent a 10 min trial period with a 3.5 min baseline period followed by 5-foot shocks of 0.9 mA intensity paired with an auditory tone. The auditory tone (5 s duration) preceded the foot shocks (200 ms duration). Equipment was cleansed with 70% ethanol between animal trials. On Day 2, mice were placed in the same context chamber as Day 1 and freezing behavior was calculated for a trial period of 5 min. Equipment was cleansed with 70% ethanol across trials. On Day 3, white plexi-glass inserts were placed in the test chamber to simulate a novel context environment. During the 5 min trial period 3 auditory tones were delivered to test cued memory.

Chemicals

Chemicals for ACSF, NMDG, sucrose (S0389), and picrotoxin (P1675) were obtained from Sigma-Aldrich. NMDG (M2004), KCl (P3911), NaH₂PO₄ (S9638), NaHCO₃ (S6014), HEPES (H3375), glucose (G8270), sodium ascorbate (A4034), Thiourea (T8656), sodium pyruvate (P2256), MgCl₂ (M2670),

CaCl₂ (C8106), NaCl (S7653), MgSO₄ (M1880), DHPG (0342) and CGP-55845 (1248), was ordered from Tocris Bioscience. HCl (SA49) was obtained from Fisher Scientific.

Statistical Analysis

Statistical Analyses and graphical data formatting were performed using GraphPad Prism 10 or Origin Pro 8 software. All data distributions were tested for normality using the Shapiro-Wilk test. Normal data distributions underwent parametric Unpaired *t*-test analysis for sample sizes ($N > 7$). For skewed distributions or sample sizes ($N < 7$) the non-parametric Mann-Whitney test was applied. For behavioral experiments, the Sidak's multiple comparison test was implemented for Day 1 of the contextual fear conditioning paradigm. The CalEx rescue experiments were analyzed using One-way ANOVA followed by post-hoc Tukey's multiple comparisons test when statistical significant interaction was detected. Statistical significance was determined for p values < 0.05 associated with the statistical analysis test applied. All experimental data collection and analysis was performed in a blind-manner.

Data availability

RNA sequencing data will be uploaded to dbGAP upon publication. This study does not report original code. Information required to reanalyze data reported is available from the lead contact upon request.

Acknowledgements

We thank the Weill Cornell Medicine Genomics and Fluorescence Activated Cell Sorting Core facilities for providing experimental consultation, assistance and results. We also thank Jens Lykke-Andersen for generously providing the anti-UPF2 antibody. We thank Natalie Wayland and Kelsey Lysek for support maintaining the mouse colonies and Mars Reynoso for performing pilot immunostainings.

Additional information

Funding

This work is supported by 1R01MH129797-01A1 grant to D.C., R01MH137503 grant to K.T. and M.F.W., R01MH125772 grant to P.E.C, and the Leon Levy Foundation Scholarship in Neuroscience to P.J.L.

Author contributions

D.C. and P.J.L conceived of the project, designed experiments, and wrote the manuscript with input from all authors. P.J.L performed majority of the experiments including, astrocyte cell selection, electrophysiology, calcium imaging, stereotaxic surgeries, behavioral tests, immunostainings, Imaris analyses, and executed associated analyses. A.D. performed Imaris analyses and associated immunostainings. E.B.A. supported behavioral tests. K.T. performed RNA-seq and NMD inducing feature analyses with supervision from M.W. Support for two-photon microscopy experiments was provided by P.E.C.

Declaration of generative AI

Generative AI was not implemented in the writing or analytical aspects of the study.

Funding

Funder	Grant reference number	Author
HHS NIH National Institute of Mental Health (NIMH)	1R01MH129797-01A1	Dilek Colak


HHS NIH National Institute of Mental Health (NIMH)	R01MH137503	Miles F Wilkinson
HHS NIH National Institute of Mental Health (NIMH)	R01MH125772	Pablo E Castillo
Leon Levy Foundation (LLF)		Pablo J Lituma

Author ORCID iDs


Pablo J Lituma:  <https://orcid.org/0000-0001-8442-3622>


Kun Tan:  <https://orcid.org/0000-0002-8567-7795>


Miles F Wilkinson:  <https://orcid.org/0000-0002-6416-3058>


Dilek Colak:  <https://orcid.org/0000-0003-4928-3999>


Additional files


Supplemental Figures.  Figures S1-S7 with associated Figure Legends.

Supplemental Table S1.  Gene List of Upregulated and Downregulated DEGs.

Supplemental Table S2.  NMD inducing feature analysis of DEGs.

Supplemental Video S1.  Elevated calcium transients in *Upf2* cKO astrocytes and restoration of calcium events in CalEx astrocytes.

Supplemental Video S2.  Elevated calcium transients in *Upf2* cKO astrocytes and restoration of calcium events in CalEx astrocytes.

Supplemental Video S3.  Elevated calcium transients in *Upf2* cKO astrocytes and restoration of calcium events in CalEx astrocytes.

References

- Bushong EA,** Martone ME, Jones YZ, Ellisman MH (2002) Protoplasmic astrocytes in CA1 stratum radiatum occupy separate anatomical domains. *J Neurosci* **22**:183-192 <https://doi.org/10.1523/jneurosci.22-01-00183.2002> | [PubMed](#)
- Oberheim NA,** et al. (2009) Uniquely hominid features of adult human astrocytes. *J Neurosci* **29**:3276-3287 <https://doi.org/10.1523/jneurosci.4707-08.2009> | [PubMed](#)
- Volterra A,** Meldolesi J (2005) Astrocytes, from brain glue to communication elements: the revolution continues. *Nat Rev Neurosci* **6**:626-640 <https://doi.org/10.1038/nrn1722> | [PubMed](#)
- Haydon PG,** Carmignoto G (2006) Astrocyte control of synaptic transmission and neurovascular coupling. *Physiol Rev* **86**:1009-1031 <https://doi.org/10.1152/physrev.00049.2005> | [PubMed](#)
- Perea G,** Navarrete M, Araque A (2009) Tripartite synapses: astrocytes process and control synaptic information. *Trends Neurosci* **32**:421-431 <https://doi.org/10.1016/j.tins.2009.05.001> | [PubMed](#)
- Araque A,** et al. (2014) Gliotransmitters travel in time and space. *Neuron* **81**:728-739 <https://doi.org/10.1016/j.neuron.2014.02.007> | [PubMed](#)
- Lee JH,** et al. (2021) Astrocytes phagocytose adult hippocampal synapses for circuit homeostasis. *Nature* **590**:612-617 <https://doi.org/10.1038/s41586-020-03060-3> | [PubMed](#)
- Lee E,** et al. (2022) A distinct astrocyte subtype in the aging mouse brain characterized by impaired protein homeostasis. *Nat Aging* **2**:726-741 <https://doi.org/10.1038/s43587-022-00257-1> | [PubMed](#)
- Bassell GJ,** Kelic S (2004) Binding proteins for mRNA localization and local translation, and their dysfunction in genetic neurological disease. *Curr Opin Neurobiol* **14**:574-581 <https://doi.org/10.1016/j.conb.2004.08.010> | [PubMed](#)
- Buffington SA,** Huang W, Costa-Mattoli M (2014) Translational control in synaptic plasticity and cognitive dysfunction. *Annu Rev Neurosci* **37**:17-38 <https://doi.org/10.1146/annurev-neuro-071013-014100> | [PubMed](#)

11. Darnell JC, Klann E (2013) The translation of translational control by FMRP: therapeutic targets for FXS. *Nat Neurosci* **16**:1530-1536 <https://doi.org/10.1038/nn.3379> | PubMed
12. Gkogkas CG, et al. (2013) Autism-related deficits via dysregulated eIF4E-dependent translational control. *Nature* **493**:371-377 <https://doi.org/10.1038/nature11628> | PubMed
13. Kelleher RJ (2008) 3rd, M. F. Bear, The autistic neuron: troubled translation?. *Cell* **135**:401-406 <https://doi.org/10.1016/j.cell.2008.10.017> | PubMed
14. Liu-Yesucevitz L, et al. (2011) Local RNA translation at the synapse and in disease. *J Neurosci* **31**:16086-16093 <https://doi.org/10.1523/jneurosci.4105-11.2011> | PubMed
15. Santini E, et al. (2013) Exaggerated translation causes synaptic and behavioural aberrations associated with autism. *Nature* **493**:411-415 <https://doi.org/10.1038/nature11782> | PubMed
16. Kurosaki T, Popp MW, Maquat LE (2019) Quality and quantity control of gene expression by nonsense-mediated mRNA decay. *Nat Rev Mol Cell Biol* **20**:406-420 <https://doi.org/10.1038/s41580-019-0126-2> | PubMed
17. Doma MK, Parker R (2007) RNA quality control in eukaryotes. *Cell* **131**:660-668 <https://doi.org/10.1016/j.cell.2007.10.041> | PubMed
18. Chan WK, et al. (2007) An alternative branch of the nonsense-mediated decay pathway. *EMBO J* **26**:1820-1830 <https://doi.org/10.1038/sj.emboj.7601628> | PubMed
19. Mendell JT, Sharifi NA, Meyers JL, Martinez-Murillo F, Dietz HC (2004) Nonsense surveillance regulates expression of diverse classes of mammalian transcripts and mutes genomic noise. *Nat Genet* **36**:1073-1078 <https://doi.org/10.1038/ng1429> | PubMed
20. He F, et al. (2003) Genome-wide analysis of mRNAs regulated by the nonsense-mediated and 5' to 3' mRNA decay pathways in yeast. *Mol Cell* **12**:1439-1452 [https://doi.org/10.1016/s1097-2765\(03\)00446-5](https://doi.org/10.1016/s1097-2765(03)00446-5) | PubMed
21. Tan K, Wilkinson MF (2025) Biological roles of nonsense-mediated RNA decay: insights from the nervous system. *Curr Opin Genet Dev* **93**:102356 <https://doi.org/10.1016/j.gde.2025.102356> | PubMed
22. Tan K, et al. (2020) The role of the NMD factor UPF3B in olfactory sensory neurons. *eLife* **9** <https://doi.org/10.7554/elife.57525> | PubMed
23. Notaras M, et al. (2020) UPF2 leads to degradation of dendritically targeted mRNAs to regulate synaptic plasticity and cognitive function. *Mol Psychiatry* **25**:3360-3379 <https://doi.org/10.1038/s41380-019-0547-5> | PubMed
24. Jaffrey SR, Wilkinson MF (2018) Nonsense-mediated RNA decay in the brain: emerging modulator of neural development and disease. *Nat Rev Neurosci* **19**:715-728 <https://doi.org/10.1038/s41583-018-0079-z> | PubMed
25. Tarpey PS, et al. (2007) Mutations in UPF3B, a member of the nonsense-mediated mRNA decay complex, cause syndromic and nonsyndromic mental retardation. *Nat Genet* **39**:1127-1133 <https://doi.org/10.1038/ng2100> | PubMed
26. Laumonnier F, et al. (2010) Mutations of the UPF3B gene, which encodes a protein widely expressed in neurons, are associated with nonspecific mental retardation with or without autism. *Mol Psychiatry* **15**:767-776 <https://doi.org/10.1038/mp.2009.14> | PubMed
27. Jolly LA, Homan CC, Jacob R, Barry S, Gecz J (2013) The UPF3B gene, implicated in intellectual disability, autism, ADHD and childhood onset schizophrenia regulates neural progenitor cell behaviour and neuronal outgrowth. *Hum Mol Genet* **22**:4673-4687 <https://doi.org/10.1093/hmg/ddt315> | PubMed
28. Nguyen LS, Wilkinson MF, Gecz J (2014) Nonsense-mediated mRNA decay: inter-individual variability and human disease. *Neurosci Biobehav Rev* **46**:175-186 <https://doi.org/10.1016/j.neubiorev.2013.10.016> | PubMed
29. Addington AM, et al. (2011) A novel frameshift mutation in UPF3B identified in brothers affected with childhood onset schizophrenia and autism spectrum disorders. *Mol Psychiatry* **16**:238-239 <https://doi.org/10.1038/mp.2010.59> | PubMed

30. **Nguyen LS**, et al. (2013) Contribution of copy number variants involving nonsense-mediated mRNA decay pathway genes to neuro-developmental disorders. *Hum Mol Genet* **22**:1816-1825 <https://doi.org/10.1093/hmg/ddt035> | [PubMed](#)
31. **Tan K**, **Sebat J**, **Wilkinson MF** (2025) Cell type- and factor-specific nonsense-mediated RNA decay. *Nucleic Acids Res* **53** <https://doi.org/10.1093/nar/gkaf395> | [PubMed](#)
32. **Johnson JL**, et al. (2019) Inhibition of Upf2-Dependent Nonsense-Mediated Decay Leads to Behavioral and Neurophysiological Abnormalities by Activating the Immune Response. *Neuron* **104**:665-679.e668 <https://doi.org/10.1016/j.neuron.2019.08.027> | [PubMed](#)
33. **Mooney CM**, et al. (2017) RNA sequencing of synaptic and cytoplasmic Upf1-bound transcripts supports contribution of nonsense-mediated decay to epileptogenesis. *Sci Rep* **7**:41517 <https://doi.org/10.1038/srep41517> | [PubMed](#)
34. **Colak D**, **Ji SJ**, **Porse BT**, **Jaffrey SR** (2013) Regulation of axon guidance by compartmentalized nonsense-mediated mRNA decay. *Cell* **153**:1252-1265 <https://doi.org/10.1016/j.cell.2013.04.056> | [PubMed](#)
35. **Lin L**, et al. (2024) Epistatic interactions between NMD and TRP53 control progenitor cell maintenance and brain size. *Neuron* **112**:2157-2176.e2112 <https://doi.org/10.1016/j.neuron.2024.04.006> | [PubMed](#)
36. **Lin L**, et al. (2026) Nonsense-mediated mRNA decay orchestrates neuronal migration and cortical lamination while modulating Reelin and ciliary gene regulatory networks. *Cell Rep* **45**:117027 <https://doi.org/10.1016/j.celrep.2026.117027> | [PubMed](#)
37. **Bao J**, **Tang C**, **Yuan S**, **Porse BT**, **Yan W** (2015) UPF2, a nonsense-mediated mRNA decay factor, is required for prepubertal Sertoli cell development and male fertility by ensuring fidelity of the transcriptome. *Development* **142**:352-362 <https://doi.org/10.1242/dev.115642> | [PubMed](#)
38. **Bao J**, et al. (2016) UPF2-Dependent Nonsense-Mediated mRNA Decay Pathway Is Essential for Spermatogenesis by Selectively Eliminating Longer 3'UTR Transcripts. *PLoS Genet* **12**:e1005863 <https://doi.org/10.1371/journal.pgen.1005863> | [PubMed](#)
39. **Chousal JN**, et al. (2022) Progression of the pluripotent epiblast depends upon the NMD factor UPF2. *Development* **149** <https://doi.org/10.1242/dev.200764> | [PubMed](#)
40. **Thoren LA**, et al. (2010) UPF2 is a critical regulator of liver development, function and regeneration. *PLoS One* **5**:e11650 <https://doi.org/10.1371/journal.pone.0011650> | [PubMed](#)
41. **Weischenfeldt J**, et al. (2008) NMD is essential for hematopoietic stem and progenitor cells and for eliminating by-products of programmed DNA rearrangements. *Genes Dev* **22**:1381-1396 <https://doi.org/10.1101/gad.468808> | [PubMed](#)
42. **Srinivasan R**, et al. (2016) New Transgenic Mouse Lines for Selectively Targeting Astrocytes and Studying Calcium Signals in Astrocyte Processes In Situ and In Vivo. *Neuron* **92**:1181-1195 <https://doi.org/10.1016/j.neuron.2016.11.030> | [PubMed](#)
43. **Chung WS**, et al. (2013) Astrocytes mediate synapse elimination through MEGF10 and MERTK pathways. *Nature* **504**:394-400 <https://doi.org/10.1038/nature12776> | [PubMed](#)
44. **Allen NJ**, et al. (2012) Astrocyte glypicans 4 and 6 promote formation of excitatory synapses via GluA1 AMPA receptors. *Nature* **486**:410-414 <https://doi.org/10.1038/nature11059> | [PubMed](#)
45. **Chung WS**, **Allen NJ**, **Eroglu C** (2015) Astrocytes Control Synapse Formation, Function, and Elimination. *Cold Spring Harb Perspect Biol* **7** <https://doi.org/10.1101/cshperspect.a020370> | [PubMed](#)
46. **Malenka RC**, **Bear MF** (2004) LTP and LTD: an embarrassment of riches. *Neuron* **44**:5-21 <https://doi.org/10.1016/j.neuron.2004.09.012> | [PubMed](#)
47. **Segal M** (2005) Dendritic spines and long-term plasticity. *Nat Rev Neurosci* **6**:277-284 <https://doi.org/10.1038/nrn1649> | [PubMed](#)
48. **Nicol RA** (2017) A Brief History of Long-Term Potentiation. *Neuron* **93**:281-290 <https://doi.org/10.1016/j.neuron.2016.12.015> | [PubMed](#)

49. Bliss TV, Collingridge GL (1993) A synaptic model of memory: long-term potentiation in the hippocampus. *Nature* **361**:31-39 <https://doi.org/10.1038/361031a0> | PubMed
50. Luscher C, Huber KM (2010) Group 1 mGluR-dependent synaptic long-term depression: mechanisms and implications for circuitry and disease. *Neuron* **65**:445-459 <https://doi.org/10.1016/j.neuron.2010.01.016> | PubMed
51. Durkee C, Kofuji P, Navarrete M, Araque A (2021) Astrocyte and neuron cooperation in long-term depression. *Trends Neurosci* **44**:837-848 <https://doi.org/10.1016/j.tins.2021.07.004> | PubMed
52. Khan ZU, Martin-Montanez E, Baxter MG (2011) Visual perception and memory systems: from cortex to medial temporal lobe. *Cell Mol Life Sci* **68**:1737-1754 <https://doi.org/10.1007/s00018-011-0641-6> | PubMed
53. Liu C, et al. (2025) Hippocampus alters visual representation to encode new memory. *Cell Rep* **44**:115594 <https://doi.org/10.1016/j.celrep.2025.115594> | PubMed
54. Preston AR, Eichenbaum H (2013) Interplay of hippocampus and prefrontal cortex in memory. *Curr Biol* **23**:R764-773 <https://doi.org/10.1016/j.cub.2013.05.041> | PubMed
55. Mederos S, et al. (2021) GABAergic signaling to astrocytes in the prefrontal cortex sustains goal-directed behaviors. *Nat Neurosci* **24**:82-92 <https://doi.org/10.1038/s41593-020-00752-x> | PubMed
56. Allen M, et al. (2022) Astrocytes derived from ASD individuals alter behavior and destabilize neuronal activity through aberrant Ca(2+) signaling. *Mol Psychiatry* **27**:2470-2484 <https://doi.org/10.1038/s41380-022-01486-x> | PubMed
57. Barrio-Alonso E, et al. (2023) Circadian protein TIMELESS regulates synaptic function and memory by modulating cAMP signaling. *Cell Rep* **42**:112375 <https://doi.org/10.1016/j.celrep.2023.112375> | PubMed
58. Cho WH, et al. (2022) Hippocampal astrocytes modulate anxiety-like behavior. *Nat Commun* **13**:6536 <https://doi.org/10.1038/s41467-022-34201-z> | PubMed
59. Walf AA, Frye CA (2007) The use of the elevated plus maze as an assay of anxiety-related behavior in rodents. *Nat Protoc* **2**:322-328 <https://doi.org/10.1038/nprot.2007.44> | PubMed
60. Soto JS, et al. (2024) Astrocyte Gi-GPCR signaling corrects compulsive-like grooming and anxiety-related behaviors in Sapap3 knockout mice. *Neuron* **112**:3412-3423.e3416 <https://doi.org/10.1016/j.neuron.2024.07.019> | PubMed
61. Soto JS, et al. (2023) Astrocyte-neuron subproteomes and obsessive-compulsive disorder mechanisms. *Nature* **616**:764-773 <https://doi.org/10.1038/s41586-023-05927-7> | PubMed
62. Pakan JM, et al. (2016) Behavioral-state modulation of inhibition is context-dependent and cell type specific in mouse visual cortex. *eLife* **5** <https://doi.org/10.7554/eLife.14985> | PubMed
63. Haydon PG, Nedergaard M (2014) How do astrocytes participate in neural plasticity?. *Cold Spring Harb Perspect Biol* **7** <https://doi.org/10.1101/cshperspect.a020438> | PubMed
64. Liu JH, et al. (2022) Distinct roles of astroglia and neurons in synaptic plasticity and memory. *Mol Psychiatry* **27**:873-885 <https://doi.org/10.1038/s41380-021-01332-6> | PubMed
65. Cruz APM, Castro-Gomes V, Landeira-Fernandez J (2024) An animal model of trait anxiety: Carioca high freezing rats as a model of generalized anxiety disorder. *Personal Neurosci* **7**:e6 <https://doi.org/10.1017/pen.2023.6> | PubMed
66. Tan K, Stupack DG, Wilkinson MF (2022) Nonsense-mediated RNA decay: an emerging modulator of malignancy. *Nat Rev Cancer* **22**:437-451 <https://doi.org/10.1038/s41568-022-00481-2> | PubMed
67. Toma KG, Rebbapragada I, Durand S, Lykke-Andersen J (2015) Identification of elements in human long 3' UTRs that inhibit nonsense-mediated decay. *RNA* **21**:887-897 <https://doi.org/10.1261/rna.048637.114> | PubMed
68. Hogg JR, Goff SP (2010) Upf1 senses 3'UTR length to potentiate mRNA decay. *Cell* **143**:379-389 <https://doi.org/10.1016/j.cell.2010.10.005> | PubMed

69. Huang L, et al. (2018) A Upf3b-mutant mouse model with behavioral and neurogenesis defects. *Mol Psychiatry* **23**:1773-1786 <https://doi.org/10.1038/mp.2017.173> | PubMed
70. Rebbapragada I, Lykke-Andersen J (2009) Execution of nonsense-mediated mRNA decay: what defines a substrate?. *Curr Opin Cell Biol* **21**:394-402 <https://doi.org/10.1016/j.ceb.2009.02.007> | PubMed
71. Eberle AB, Stalder L, Mathys H, Orozco RZ, Muhlemann O (2008) Posttranscriptional gene regulation by spatial rearrangement of the 3' untranslated region. *PLoS Biol* **6**:e92 <https://doi.org/10.1371/journal.pbio.0060092> | PubMed
72. Singh G, Rebbapragada I, Lykke-Andersen J (2008) A competition between stimulators and antagonists of Upf complex recruitment governs human nonsense-mediated mRNA decay. *PLoS Biol* **6**:e111 <https://doi.org/10.1371/journal.pbio.0060111> | PubMed
73. Bazargani N, Attwell D (2016) Astrocyte calcium signaling: the third wave. *Nat Neurosci* **19**:182-189 <https://doi.org/10.1038/nn.4201> | PubMed
74. Ahrens MB, Khakh BS, Poskanzer KE (2024) Astrocyte Calcium Signaling. *Cold Spring Harb Perspect Biol* **16** <https://doi.org/10.1101/cshperspect.a041353> | PubMed
75. Allen NJ (2014) Astrocyte regulation of synaptic behavior. *Annu Rev Cell Dev Biol* **30**:439-463 <https://doi.org/10.1146/annurev-cellbio-100913-013053> | PubMed
76. Hausteil MD, et al. (2014) Conditions and constraints for astrocyte calcium signaling in the hippocampal mossy fiber pathway. *Neuron* **82**:413-429 <https://doi.org/10.1016/j.neuron.2014.02.041> | PubMed
77. Glaum SR, Holzwarth JA, Miller RJ (1990) Glutamate receptors activate Ca²⁺ mobilization and Ca²⁺ influx into astrocytes. *Proc Natl Acad Sci U S A* **87**:3454-3458 <https://doi.org/10.1073/pnas.87.9.3454> | PubMed
78. Oliveira JF, Sardinha VM, Guerra-Gomes S, Araque A, Sousa N (2015) Do stars govern our actions? Astrocyte involvement in rodent behavior. *Trends Neurosci* **38**:535-549 <https://doi.org/10.1016/j.tins.2015.07.006> | PubMed
79. Yu X, et al. (2018) Reducing Astrocyte Calcium Signaling In Vivo Alters Striatal Microcircuits and Causes Repetitive Behavior. *Neuron* **99**:1170-1187.e1179 <https://doi.org/10.1016/j.neuron.2018.08.015> | PubMed
80. Yu X, Moye SL, Khakh BS (2021) Local and CNS-Wide Astrocyte Intracellular Calcium Signaling Attenuation In Vivo with CalEx(flox) Mice. *J Neurosci* **41**:4556-4574 <https://doi.org/10.1523/jneurosci.0085-21.2021> | PubMed
81. Wang Q, et al. (2021) Impaired calcium signaling in astrocytes modulates autism spectrum disorder-like behaviors in mice. *Nat Commun* **12**:3321 <https://doi.org/10.1038/s41467-021-23843-0> | PubMed
82. Henneberger C, et al. (2020) LTP Induction Boosts Glutamate Spillover by Driving Withdrawal of Perisynaptic Astroglia. *Neuron* **108**:919-936.e911 <https://doi.org/10.1016/j.neuron.2020.08.030> | PubMed
83. Theodosis DT, Poulain DA, Oliet SH (2008) Activity-dependent structural and functional plasticity of astrocyte-neuron interactions. *Physiol Rev* **88**:983-1008 <https://doi.org/10.1152/physrev.00036.2007> | PubMed
84. Glykos V, Pavon MV, Goda Y (2025) Cell biology of astrocytic adhesive interactions and signaling pathways in regulating neuronal circuits. *Curr Opin Neurobiol* **93**:103037 <https://doi.org/10.1016/j.conb.2025.103037> | PubMed
85. Bernardinelli Y, et al. (2014) Activity-dependent structural plasticity of perisynaptic astrocytic domains promotes excitatory synapse stability. *Curr Biol* **24**:1679-1688 <https://doi.org/10.1016/j.cub.2014.06.025> | PubMed
86. Tancredi V, et al. (2000) The inhibitory effects of interleukin-6 on synaptic plasticity in the rat hippocampus are associated with an inhibition of mitogen-activated protein kinase ERK. *J Neurochem* **75**:634-643 <https://doi.org/10.1046/j.1471-4159.2000.0750634.x> | PubMed

87. Nishiyama H, Knopfel T, Endo S, Itohara S (2002) Glial protein S100B modulates long-term neuronal synaptic plasticity. *Proc Natl Acad Sci U S A* **99**:4037-4042 <https://doi.org/10.1073/pnas.052020999> | PubMed
88. Brozzi F, Arcuri C, Giambanco I, Donato R (2009) S100B Protein Regulates Astrocyte Shape and Migration via Interaction with Src Kinase: IMPLICATIONS FOR ASTROCYTE DEVELOPMENT, ACTIVATION, AND TUMOR GROWTH. *J Biol Chem* **284**:8797-8811 <https://doi.org/10.1074/jbc.m805897200> | PubMed
89. Zou Z, et al. (2022) The role of S100B/RAGE-enhanced ADAM17 activation in endothelial glycocalyx shedding after traumatic brain injury. *J Neuroinflammation* **19**:46 <https://doi.org/10.1186/s12974-022-02412-2> | PubMed
90. Lynn KS, Peterson RJ, Koval M (2020) Ruffles and spikes: Control of tight junction morphology and permeability by claudins. *Biochim Biophys Acta Biomembr* **1862**:183339 <https://doi.org/10.1016/j.bbamem.2020.183339> | PubMed
91. Cathomas F, et al. (2024) Circulating myeloid-derived MMP8 in stress susceptibility and depression. *Nature* **626**:1108-1115 <https://doi.org/10.1038/s41586-023-07015-2> | PubMed
92. Tietz S, Engelhardt B (2015) Brain barriers: Crosstalk between complex tight junctions and adherens junctions. *J Cell Biol* **209**:493-506 <https://doi.org/10.1083/jcb.201412147> | PubMed
93. Ma Z, Stork T, Bergles DE, Freeman MR (2016) Neuromodulators signal through astrocytes to alter neural circuit activity and behaviour. *Nature* **539**:428-432 <https://doi.org/10.1038/nature20145> | PubMed
94. Pascual O, et al. (2005) Astrocytic purinergic signaling coordinates synaptic networks. *Science* **310**:113-116 <https://doi.org/10.1126/science.1116916> | PubMed
95. Mariotti L, Losi G, Sessolo M, Marcon I, Carmignoto G (2016) The inhibitory neurotransmitter GABA evokes long-lasting Ca(2+) oscillations in cortical astrocytes. *Glia* **64**:363-373 <https://doi.org/10.1002/glia.22933> | PubMed
96. Durkee CA, et al. (2019) G(i/o) protein-coupled receptors inhibit neurons but activate astrocytes and stimulate gliotransmission. *Glia* **67**:1076-1093 <https://doi.org/10.1002/glia.23589> | PubMed
97. Martin-Fernandez M, et al. (2017) Synapse-specific astrocyte gating of amygdala-related behavior. *Nat Neurosci* **20**:1540-1548 <https://doi.org/10.1038/nn.4649> | PubMed
98. Tan W, et al. (2024) Anxiety control by astrocytes in the lateral habenula. *Neurosci Res* **205**:1-15 <https://doi.org/10.1016/j.neures.2024.01.006> | PubMed
99. Peyton L, et al. (2025) In vivo calcium extrusion from accumbal astrocytes reduces anxiety-like behaviors but increases compulsive-like responses and compulsive ethanol drinking in mice. *Neuropharmacology* **268**:110320 <https://doi.org/10.1016/j.neuropharm.2025.110320> | PubMed
100. Suthard RL, et al. (2023) Chronic Gq activation of ventral hippocampal neurons and astrocytes differentially affects memory and behavior. *Neurobiol Aging* **125**:9-31 <https://doi.org/10.1016/j.neurobiolaging.2023.01.007> | PubMed
101. Khakh BS, Sofroniew MV (2015) Diversity of astrocyte functions and phenotypes in neural circuits. *Nat Neurosci* **18**:942-952 <https://doi.org/10.1038/nn.4043> | PubMed
102. Huang AY, et al. (2020) Region-Specific Transcriptional Control of Astrocyte Function Oversees Local Circuit Activities. *Neuron* **106**:992-1008.e1009 <https://doi.org/10.1016/j.neuron.2020.03.025> | PubMed
103. Madisen L, et al. (2010) A robust and high-throughput Cre reporting and characterization system for the whole mouse brain. *Nat Neurosci* **13**:133-140 <https://doi.org/10.1038/nn.2467> | PubMed
104. Tan K, et al. (2021) The RhoX gene cluster suppresses germline LINE1 transposition. *Proc Natl Acad Sci U S A* **118** <https://doi.org/10.1073/pnas.2024785118> | PubMed
105. Lituma PJ, et al. (2021) Altered synaptic connectivity and brain function in mice lacking microglial adapter protein Iba1. *Proc Natl Acad Sci U S A* **118** <https://doi.org/10.1073/pnas.2115539118> | PubMed

106. Schafer DP, Lehrman EK, Heller CT, Stevens B (2014) An engulfment assay: a protocol to assess interactions between CNS phagocytes and neurons. *J Vis Exp* <https://doi.org/10.3791/51482> | PubMed

Peer reviews

Reviewer #1 (Public review):

Summary:

Lituma and colleagues investigate the role of NMD in astrocytes, an underexplored question given that prior work on NMD in the brain has focused exclusively on neurons. Using a tamoxifen-inducible, astrocyte-specific *Upf2* conditional knockout (cKO) mouse, they report that loss of astrocytic NMD causes: (1) reductions in astrocyte cell volume and surface area across hippocampus, visual cortex, and prefrontal cortex; (2) decreased excitatory synapse density, reduced dendritic spine density, and impaired synaptic engulfment; (3) deficits in basal synaptic transmission and LTP, with selective impairment of mGluR-LTD; (4) elevated spontaneous calcium transients in astrocytes; and (5) anxiety-like behavior in the elevated plus maze (EPM) and contextual fear conditioning paradigms. Transcriptomic analysis of FACS-isolated astrocytes identifies 277 differentially expressed genes, ~40% of which carry canonical NMD-inducing features, implicating pathways linked to calcium signaling, phagosome formation, and glial development. A rescue experiment using the CalEx calcium extrusion pump demonstrates partial restoration of synaptic strength and anxiety behavior when astrocytic calcium is normalized.

The study addresses an important gap in our understanding of RNA regulation in glial cells, and the overall conceptual framework is well described. The experimental design is generally appropriate, and the multi-pronged approach lends the main claims a degree of validity.

Strengths:

- (1) Novelty: This is the first study to systematically examine NMD function in astrocytes in vivo. The identification of astrocytic NMD targets via RNA-seq combined with an NMD-inducing feature classifier is a meaningful methodological contribution.
- (2) Multi-method approach: The authors combine morphological analysis (Imaris 3D reconstruction), synaptic markers (PSD-95, LAMP2 engulfment assay), spine density measurements, acute slice electrophysiology, two-photon calcium imaging, behavioral testing, and transcriptomics. The convergence across these methods strengthens confidence in the claims.

Weaknesses:

- (1) While the transcriptomic analysis is a valuable addition, the connection between specific NMD targets and the observed calcium phenotype remains largely correlational. The authors identify *Gabbr2* and *Adora1* as upregulated candidates with canonical NMD features and speculate that their elevated expression drives aberrant calcium signaling. However, no validation (e.g., qRT-PCR or protein-level confirmation) of these candidates is presented. The mechanistic pathway between NMD disruption and elevated calcium is thus inferred from pathway analysis rather than demonstrated. This is a significant gap between the transcriptomic and physiological arms of the study, and the authors should be more explicit about this limitation or, ideally, provide at least one validated target.
- (2) The reduction in astrocyte surface area in cKO mice is interpreted as contributing to reduced synapse contact and engulfment capacity. This is a reasonable hypothesis, but the study does not directly demonstrate that reduced astrocyte territory correlates with reduced

synaptic coverage at the level of individual cells or brain regions. The temporal sequence of these events is unknown. Do morphological deficits precede synaptic changes? Clarification and qualification of this causal chain in the Discussion would strengthen the manuscript.

(3) LFS-induced LTD is unaffected, while mGluR-LTD is reduced. This is intriguing and potentially informative about astrocyte contributions to distinct LTD mechanisms, but the difference receives limited discussion. Given the relevance of mGluR signaling to calcium dynamics and the identified pathway enrichments (GPCR signaling), this specificity deserves more attention.

(4) The CTRL + CalEx condition is included in the EPM experiment but not in the electrophysiology or calcium imaging experiments, making it difficult to fully assess whether CalEx itself has off-target effects on synaptic transmission or anxiety in wild-type animals. The CTRL + CalEx EPM data (Figure 7F) appears to show a modest reduction in open arm time relative to CTRL, which, if robust, would suggest that excessive calcium reduction in astrocytes is also anxiogenic. This finding would be physiologically relevant and deserves comment.

<https://doi.org/10.7554/eLife.111940.1.sa3>

Reviewer #2 (Public review):

Astrocytes are highly responsive to their environment and play a range of critical roles in brain function. Lituma et al. theorize that one mediator of that responsiveness is the regulation of RNA stability. They therefore undertake an assessment of astrocytes missing Upf2, a protein required for mRNA degradation via nonsense-mediated decay. This is an interesting study, approaching astrocyte biology from a novel angle. The authors take on an ambitious set of experiments, spanning morphological assessment, synaptic engulfment, electrophysiology, behavior, and calcium imaging.

The authors show convincing data that knocking out Upf2 in astrocytes impairs synaptic plasticity, affects behavior, and changes the complement of astrocytic mRNA. These results, in and of themselves, are intriguing and suggest that NMD is an important biological process in astrocytes, warranting further study.

My primary concern is whether the authors may be largely studying dying cells. The idea that NMD disruption has a dramatic effect on astrocyte morphology is an intriguing idea, but it is not fully established here. The nuclei in the example cKO morphology images appear small and/or fragmented. This raises concerns that the authors did not ensure that they had the full 3D morphology of the astrocyte in the section, and the cell is in part cut off, which would compromise any data on the morphology. The authors state that the tissue was sectioned at 70 μm . The diameter of an astrocyte in the adult mouse brain is typically between 50 and 70 μm . Unless astrocytes are perfectly positioned in the center of the slice, at this thickness, the majority of astrocytes will almost certainly be partially cut off. More detail on how cells were chosen and what quality control metrics were implemented would alleviate concerns here. An alternative possible explanation for these small/fragmented nuclei is that cKO astrocytes may be unhealthy to the point that they are actively dying. Using the transgenic ZsGreen label, the authors state that they observe a size change (Figure S4); this is not readily apparent and is not quantified in any way. It does appear from these images that there may be a loss of some astrocytes; cell death, which would also be an interesting finding, is a fundamentally different process than morphologic restructuring in living cells. The authors do attempt to count astrocytes (Figure S6B), but do so with GFAP. This is a fundamentally flawed approach. Because GFAP is not readily detectable in most healthy astrocytes in most gray matter regions, GFAP should not be used to quantify astrocyte numbers; this experiment should be repeated with a better marker, such as Aldh1l1, Sox9, etc.

Synaptic engulfment: This is an extraordinarily high degree of engulfment in the control animals compared to many published studies, leading to concern as to the technical approach. Indeed, the overall low level of PSD-95 signal in control conditions in adult mice is concerning as to the technical accuracy of the approach. It is unclear exactly how the investigators labeled the astrocytes; presumably via the ZsGreen label, but it is never stated, and the only images shown are the highly processed Imaris renderings. The small astrocytic processes, or leaflets, that make up the vast majority of the astrocytic arbor are on the order of 100nm in diameter. The processes shown in Figure 2B are, according to the scale bar, at least 20x that size. It is difficult to have much faith in these results as currently presented.

The signal-to-noise ratio of the GCaMP experiments is worryingly low, likely responsible for the abnormally low dF/F in all conditions and the lack of significant change between control and CalEx, when control astrocytes should show a much higher GCaMP signal than any CalEx-expressing astrocyte. That said, the higher Ca^{++} in Upf2 KO astrocytes is intriguing. Given the roles of elevated calcium in cell death, this may reflect cells that are unhealthy to the point that they are starting to die.

The authors conduct a FACS-based analysis of astrocytic mRNA from control vs Upf2-KO, with intriguing results. An important caveat, though, is that a large amount of astrocytic mRNA is in the processes. If mRNA stability is being actively and rapidly regulated, it seems likely that the mRNA in the processes would be the most relevant population of regulated mRNA. FACS-based approaches to astrocyte purification will, as robustly shown elsewhere, strip off those processes. Particularly given that the authors have shown that the processes may be the most actively changing astrocytic compartment with Upf2 KO, this is a strange choice of technique vs. something like Ribotag that would preserve the mRNA in processes. At least, there should be some discussion regarding using FACS for this analysis and the consequences for profiling mRNA in astrocytic processes.

Minor points:

(1) The use of the Aldh111-CreER mouse is a strong choice and has been shown to be highly astrocyte-specific. Combining that transgenic mouse with viruses driven by different forms of the GFAP promoter is quite bizarre in several ways. First, GFAP-dependent AAVs have been shown repeatedly to have significant neuronal leak. Second, these mice are, in all cases, receiving two different viruses, driven by different forms of the GFAP promoter, and the non-Cre virus is not Cre-dependent (vs. a much more standard approach of using a Cre-dependent second virus to ensure that all analyzed cells received both viruses). The authors mention that "this experimental design ensures that phenotypes are not caused by an acute effect of tamoxifen." It is certainly true that tamoxifen is not a biologically neutral molecule. However, the mice still receive tamoxifen, both in these morphology virus experiments and in almost all other experiments. This experimental approach is not inherently bad, nor does it necessarily invalidate the data (although the near-certain neuronal contamination due to the GFAP promoter-driven viruses is a concern). It is, however, convoluted in ways that appear unnecessary. If there is a strong rationale for this approach beyond the tepid explanation already present, it should be explicitly mentioned.

(2) The characterization of the knockout is incomplete. While the authors should be applauded for their attempts to phenotype the cells in which they observe Cre-mediated recombination, there are issues with their technical approach. Most importantly, and an issue that affects other analyses in the paper as well: the vast majority of astrocytes in the healthy cortex do not express GFAP. Therefore, using GFAP to claim high astrocyte specificity and efficiency is a fundamentally flawed approach. Second, MBP is a myelin marker, not a cytoplasmic marker, and would not successfully colocalize with a cytoplasmic marker like ZsGreen even if recombination in oligodendrocytes did occur. Third, recombination at one set of LoxP sites is not a reliable indicator of recombination at other sites. Recombination efficiency is highly dependent on the spacing between the LoxP sites and cannot be reliably

extrapolated to other floxed genes without validation. Finally, the most likely culprit for off-target recombination with Aldh111-CreERT2 (or other astrocyte-selective Cres, and certainly the GFAP-based viral promoters) is neurons, which the investigators did not test for. Neuronal Aldh111-CreERT2 leak is most likely to occur in the hippocampus. With the images shown in Fig S3, it is unclear whether it is possible to convincingly colocalize Upf2 staining with a cytosolic marker of all astrocytes, such as Aldh111 or S100b, but such data would be more appropriate. An alternative approach to validation would be in situ hybridization.

(3) Supplementary Table 2 should include gene IDs, not just Ensemble IDs.

(4) It is not fully clear what the investigators are denoting as a spine in Figure 2E; the two images do not appear to have the large degree of difference that the quantification suggests. The oversaturation of the signal complicates assessment.

(4) A more detailed discussion of the rationale behind the timeline would be helpful. What is the half-life of Upf2, and how rapidly do NMD genes build up upon Upf2 disruption? In particular, in the case of virus experiments, the timeline is quite fast: ~2.5 weeks from injection to analysis. ssAAV expression takes over a week to reach appreciable levels.

<https://doi.org/10.7554/eLife.111940.1.sa2>

Reviewer #3 (Public review):

Summary:

The authors investigate mRNA targets of the nonsense-mediated decay (NMD) pathway in astrocytes and link the dysfunction of NMD in astrocytes to aberrant synaptic transmission that has downstream effects on behavior. Specifically, they find a link between the aberrant synaptic transmission with elevated spontaneous calcium signaling in astrocytes, and functionally they demonstrate that manipulating astrocyte calcium signaling with CalEx modulates astrocyte calcium signaling towards wildtype levels and improves anxiety behavior. They investigate the astrocyte calcium signaling changes in Upf2 conditional knockout mice in several brain regions that have been linked to anxiety behavior, including the hippocampus and prefrontal cortex. They also observe aberrant astrocyte calcium signaling in the visual cortex, demonstrating that dysfunction of the NMD pathway in astrocytes has widespread effects on synaptic transmission in various brain regions. This work identifies, through RNA-Sequencing, potential mRNA targets of NMD in astrocytes, and shows that pathway enrichment of these targets highlights calcium signaling. Altogether, this work highlights the importance of the basic cellular process of NMD in astrocytes, which are known to have extensive local translation of proteins in their perisynaptic processes. NMD may be particularly important in astrocytes due to their intimate association of processes with neuronal synapses, and the authors suggest that alterations to NMD function in astrocytes may be an important avenue for future investigation in neurodevelopmental disorders.

Strengths:

Altogether, this work is a critical foundation for future research into astrocyte contributions to neurodevelopmental disorders. The authors do a thorough characterization of astrocyte conditional Upf2 knockout mice in several brain regions. They present a complete story that connects molecular events (NMD pathway regulation of mRNA degradation) to astrocyte regulation of circuit activity to organismal behavior. The electrophysiological analysis is thorough, and the manipulation of calcium activity ties astrocyte calcium activity to anxiety behavior. The RNA-sequencing dataset is useful to the scientific community and provides a resource of candidate molecules that might be dysregulated in neurodevelopmental disorders.

Weaknesses:

The study suffers from some overstated claims and a lack of statistical rigor in some experiments, as detailed below.

(1) The title states that "Astrocytic Nonsense-mediated mRNA decay regulates calcium signaling to support synapse function and restrain anxiety". The term "restrain anxiety" implies that the NMD pathway has a direct effect on a molecular switch to control anxiety. Anxiety behavior is a complicated process, controlled by many biological phenomena and synaptic transmission in the circuit as a whole, and is not directly linked to a specific NMD mRNA target. This title is overstating the findings of the study.

(2) In general, the first figures (1-2) suffer from low power ($N = 3$) and statistical rigor. The statistics are inflated by analyzing individual fields of view and per-cell data rather than performing the statistics on the average of biological replicates. It is preferable to show the biological replicate data so that readers can observe the natural biological variability between replicates.

(3) The claim that astrocytes have decreased engulfment of synapses in the *Upf2* conditional knockout mice is not strongly substantiated by the data. The resolution of confocal microscopy and the static nature of histological images make it difficult to measure synaptic engulfment as an active process. Additionally, the metric of quantifying the % occupancy of PSD95 puncta within the total astrocyte volume may be skewed due to overall differences in cell size (shown in Figure 1). There is not much discussion of how a decrease in astrocyte engulfment of synapses may lead to decreased synapse number. To the contrary, one might expect decreased engulfment to result in increased synapse density.

(4) The authors use *Gfap* as a marker to count astrocyte cell number and assess if there are changes in cell number between genotypes (Figure S6). However, *Gfap* does not label all astrocytes in the cortex and, in fact, is rather an aberrantly expressed marker in conditions of inflammation, as opposed to the hippocampus, where *Gfap* is basally expressed in all astrocytes. In the cortex, there seems to be a trend for reduced *Gfap* in the conditional knockout mice, which may suggest differences in astrocyte molecular signatures rather than cell numbers. Another astrocyte marker, like *Aldh1L1*, will be more accurate to assess this question histologically.

(5) The authors state that "Preventing abnormally high basal calcium activity in NMD-deficient astrocytes restores normal excitatory synapse function...". However, this claim is not substantiated by the data. *CalEx* manipulation certainly shifts the input-output curve but does not restore to wildtype baseline levels (Figure 6E). Additionally, synapse number does not appear to be restored to wildtype levels (Figure 6D - although the p-value for this comparison is now shown). The investigators do observe improvements in anxiety phenotypes, suggesting there is some modulation of circuit activity, but the claim that *CalEx* manipulation restores baseline synaptic transmission is not supported.

<https://doi.org/10.7554/eLife.111940.1.sa1>

Author response:

We thank the reviewers for their careful reading of our manuscript and for providing positive, constructive feedback. In particular, we thank the reviewers highlighting the several strengths of our study.

To address the reviewers' major concerns, we will revise the presentation of our main findings (specifically data/animal vs data/ROI), provide more clarity in the Results, Methods, and Discussion sections, and modify the title to better reflect these nuances.

Additionally, we will perform the following new experiments:

- (1) Astrocytic Marker Validation: To further confirm comparable astrocyte cell counts between the CTRL and *Upf2*-cKO conditions, we will perform immunostainings using Aldh1L1, Sox9, or S100b instead of GFAP.
- (2) NMD Candidate Validation: To validate top candidate NMD target transcripts, we will perform immunostainings or qRT-PCR for *Gabbr2*, *Adora1*, *S100b*, or *Cldn9*.
- (3) Sample Size Expansion: To strengthen the morphological and PSD-95 quantifications, we will increase the sample size (*N*) by incorporating additional animals.
- (4) Mechanistic Timeline & Phenotype Linkage: We value the reviewer's comment regarding the timeline of morphological and Ca²⁺ phenotypes. To gain insight into whether these phenotypes are independent or linked, we will perform 3D reconstructions in CalEx conditions to assess whether Ca²⁺ restoration rescues astrocyte morphology in *Upf2*-cKO mice. This will allow us to determine if increased Ca²⁺ activity is upstream of the morphological alterations. Taken together, we believe that incorporating these manuscript revisions will strengthen the clarity and conclusions of our work. We thank the reviewers for their time and careful evaluation of our study.

<https://doi.org/10.7554/eLife.111940.1.sa0>